



HAL
open science

A Study of Daytime Convective Vortices and Turbulence in the Martian Planetary Boundary Layer Based on Half-a-Year of InSight Atmospheric Measurements and Large-Eddy Simulations

A Spiga, N Murdoch, R Lorenz, F Forget, C Newman, S Rodriguez, J Pla-garcia, D Moreiras, D Banfield, C Perrin, et al.

► To cite this version:

A Spiga, N Murdoch, R Lorenz, F Forget, C Newman, et al.. A Study of Daytime Convective Vortices and Turbulence in the Martian Planetary Boundary Layer Based on Half-a-Year of InSight Atmospheric Measurements and Large-Eddy Simulations. *Journal of Geophysical Research. Planets*, 2021, 126 (1), pp.e2020JE006511. 10.1029/2020je006511 . hal-03657983v2

HAL Id: hal-03657983

<https://u-paris.hal.science/hal-03657983v2>

Submitted on 3 May 2022

HAL is a multi-disciplinary open access archive for the deposit and dissemination of scientific research documents, whether they are published or not. The documents may come from teaching and research institutions in France or abroad, or from public or private research centers.

L'archive ouverte pluridisciplinaire **HAL**, est destinée au dépôt et à la diffusion de documents scientifiques de niveau recherche, publiés ou non, émanant des établissements d'enseignement et de recherche français ou étrangers, des laboratoires publics ou privés.

A Study of Daytime Convective Vortices and Turbulence in the Martian Planetary Boundary Layer Based on Half-a-Year of InSight Atmospheric Measurements and Large-Eddy Simulations

A. Spiga^{1,2} , N. Murdoch³ , R. Lorenz⁴ , F. Forget¹ , C. Newman⁵ , S. Rodriguez⁶ , J. Pla-Garcia⁷ , D. Viúdez Moreiras⁷ , D. Banfield⁸, C. Perrin⁶ , N. T. Mueller⁹ , M. Lemmon¹⁰ , E. Millour¹ , and W. B. Banerdt¹¹

Key Points:

- We study daytime turbulence with InSight atmospheric measurements and large-eddy simulations
- We identify convective cells, as well as numerous convective vortices following a power law of exponent 3.4
- Seasonal variability of convective vortices controlled by wind advection and conversely turbulent gustiness correlated with surface temperature

Correspondence to:

A. Spiga,
aymeric.spiga@sorbonne-universite.fr

Citation:

Spiga, A., Murdoch, N., Lorenz, R., Forget, F., Newman, C., Rodriguez, S., et al. (2021). A study of daytime convective vortices and turbulence in the Martian planetary boundary layer based on half-a-year of InSight atmospheric measurements and large-eddy simulations. *Journal of Geophysical Research: Planets*, 126, e2020JE006511. <https://doi.org/10.1029/2020JE006511>

Received 4 MAY 2020
Accepted 8 NOV 2020

¹Laboratoire de Météorologie Dynamique/Institut Pierre-Simon Laplace (LMD/IPSL), Centre National de la Recherche Scientifique (CNRS), Sorbonne Université, Paris, France, ²Institut Universitaire de France (IUF), Paris, France, ³Institut Supérieur de l'Aéronautique et de l'Espace (ISAE-SUPAERO), Toulouse, France, ⁴Johns Hopkins Applied Physics Laboratory, Laurel, MD, USA, ⁵Aeolis Research, Chandler, AZ, USA, ⁶Institut de physique du globe de Paris, CNRS, Université de Paris, Paris, France, ⁷Centro de Astrobiología (CSIC-INTA), Madrid, Spain, ⁸Cornell Center for Astrophysics and Planetary Science, Cornell University, Ithaca, NY, USA, ⁹German Aerospace Center (DLR), Institute of Planetary Research, Berlin, Germany, ¹⁰Space Science Institute, Boulder, CO, USA, ¹¹Jet Propulsion Laboratory, California Institute of Technology, Pasadena, CA, USA

Abstract Studying the atmospheric planetary boundary layer (PBL) is crucial to understand the climate of a planet. The meteorological measurements by the instruments onboard InSight at a latitude of 4.5°N make a unique rich data set to study the active turbulent dynamics of the daytime PBL on Mars. Here we use the high-sensitivity continuous pressure, wind, and temperature measurements in the first 400 sols of InSight operations (from northern late winter to midsummer) to analyze wind gusts, convective cells, and vortices in Mars' daytime PBL. We compare InSight measurements to turbulence-resolving large-eddy simulations (LES). The daytime PBL turbulence at the InSight landing site is very active, with clearly identified signatures of convective cells and a vast population of 6,000 recorded vortex encounters, adequately represented by a power law with a 3.4 exponent. While the daily variability of vortex encounters at InSight can be explained by the statistical nature of turbulence, the seasonal variability is positively correlated with ambient wind speed, which is supported by LES. However, wind gustiness is positively correlated to surface temperature rather than ambient wind speed and sensible heat flux, confirming the radiative control of the daytime Martian PBL; and fewer convective vortices are forming in LES when the background wind is doubled. Thus, the long-term seasonal variability of vortex encounters at the InSight landing site is mainly controlled by the advection of convective vortices by ambient wind speed. Typical tracks followed by vortices forming in the LES show a similar distribution in direction and length as orbital imagery.

Plain Language Summary InSight is a lander sent to the surface of Mars with a weather station capable, like never before, to measure pressure, temperature, and winds continuously and at high cadence. We use this InSight atmospheric data set acquired over half a Martian year, along with computer simulations, to study the intense turbulence that develops in the daytime hours on Mars. InSight detects periodic variations in the measurements of the weather station, corresponding to air motions driven by convection. We also detect a large population of 6,000 whirlwinds passing close to the InSight lander and causing the pressure at the weather station to suddenly drop. The number of those whirlwind encounters varies from day to day, because of the random turbulence, and, on a seasonal basis, because of the varying ambient wind that transports the whirlwinds toward InSight. Unlike the population of whirlwinds, the strength of wind gusts follows the ground temperature varying with season. Whirlwinds also leave graffiti-like dark tracks at the surface of Mars that can be imaged by satellites in the InSight region and reproduced by our numerical simulations.

1. Introduction

Mars is a cold desert; yet its near-surface atmosphere, the so-called planetary boundary layer (PBL), is prone to strong turbulent motions in the daytime (Petrosyan et al., 2011, and references therein). Daytime turbulent motions in the thin Martian atmosphere include spectacular vortices that may appear as *dust devils* if they raise sufficient dust, strong updrafts at the borders of convective cells, and powerful wind gusts. These motions result in a mixing of heat, momentum, dust particles, and chemical species over altitudes of several kilometers above the surface, making PBL processes on Mars a crucial step to understand the meteorology and climate. The Martian PBL also exhibits interesting differences with the terrestrial PBL, notably a strong control on the daytime PBL turbulence by the near-surface atmospheric absorption of surface infrared emission (Haberle et al., 1993; Sävijärvi, 1999; Spiga et al., 2010).

Phenomena related to daytime turbulence on Mars cause pressure, wind, and temperature to fluctuate at timescales shorter than a Martian hour (defined as 1/24 of a Martian day or sol). Such signatures have been recorded in the in situ meteorological measurements of Viking (Hess et al., 1977; Tillman et al., 1994), Pathfinder (Larsen et al., 2002; Schofield et al., 1997), Phoenix (Ellehoj et al., 2010; Holstein-Rathlou et al., 2010), Spirit and Opportunity (Smith et al., 2006), and Curiosity (Kahanpää et al., 2016; Ordóñez-Etxeberria et al., 2018; Steakley & Murphy, 2016), as is summarized in the review by Martínez et al. (2017). Turbulence-resolving numerical modeling referred to as large-eddy simulations (LES) can help to make sense of the PBL events arising in time series obtained by single-station measurements (e.g., pressure drops, wind gusts, and quasi-periodic temperature fluctuations) in the broader context of convective turbulence in the PBL (see Spiga et al., 2016 for a review).

The instrumentation implemented on the InSight spacecraft, which landed on Mars on the flat plains of Elysium Planitia (4.5°N, 135.6°E) on 28 November 2018, is particularly suitable to conduct studies of PBL turbulence (Banfield et al., 2020; Banerdt et al., 2020; Spiga et al., 2018). The pressure sensor is characterized by its unprecedented sensitivity and high-frequency acquisition (Banfield et al., 2018). The wind and temperature measurements, albeit similar to the ones performed onboard Curiosity (Gómez-Elvira et al., 2012), benefit for the first time from the simultaneous use of two booms facing in opposite directions—inadvertent destruction of one of the Curiosity wind sensors by flying debris at landing produced observational biases which made only winds coming from certain directions reliably measurable (Newman et al., 2017), making the Curiosity wind retrieval challenging (Viúdez-Moreiras et al., 2019). Another key novel characteristic of InSight's in situ meteorological observations is that measurements of pressure, temperature, and wind are made continuously (Spiga et al., 2018), as they are needed to constrain the atmosphere-induced seismic noise (García et al., 2020; Kenda et al., 2017; Murdoch et al., 2017) at all times in order to assess how much of the seismic signal corresponds to the activity in the interior of Mars. Those direct atmospheric measurements are complemented by surface brightness temperature sensing (Mueller et al., 2020), color imaging (Maki et al., 2018), and, for the first time, at the surface of Mars, seismic measurements (Lognonné et al., 2020). Furthermore, solar array currents can also be used for atmospheric investigations (Lorenz et al., 2020).

The potential of InSight to study the daytime PBL turbulence was actually unveiled the very first time the pressure sensor was switched on for a 900-s test, at about 10:30 Mars local time on InSight sol 4. Figure 1 shows the occurrence of a sudden, short-duration pressure drop of amplitude 0.6 Pa, characteristic of a convective vortex, in the midst of longer, 100-s-period fluctuations of pressure of amplitude 0.1 Pa, and characteristic of convective cells.

The goal of the present study is to use InSight measurements in the first half year of operations in order to explore the atmospheric PBL dynamics in the daytime, especially convective cells and vortices, and to propose a preliminary assessment of the seasonal variability thereof and the vortex population statistics. This study focuses on PBL turbulent structures and convective vortices, regardless of whether they carry dust particles or not. The question as to whether the identified vortices in this study are carrying a sufficient amount of dust particles to be visible as dust devils in InSight's cameras is left for future studies; as is described in Banfield et al. (2020), despite extensive imaging campaigns, no dust devils were observed by InSight (this extends to the sols 0–400 spanned by the current study). The diagnostics drawn from InSight observations are compared to turbulence-resolving LES using the model described in Spiga et al. (2010).

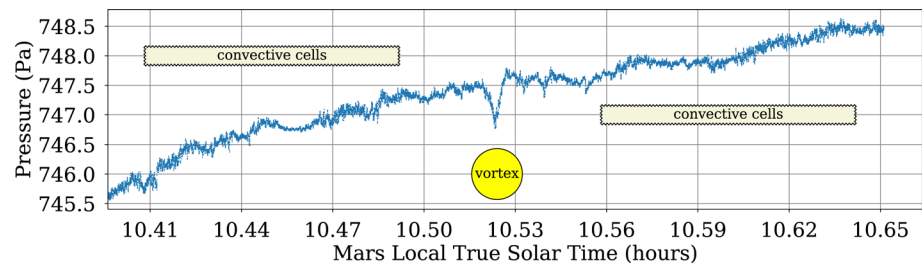


Figure 1. The first pressure measurements onboard InSight on sol 4 ($L_s = 298^\circ$, November 30, 2018) directly shows how daytime convective turbulence in the planetary boundary layer leaves distinctive signatures in the pressure time series (the time axis is the Mars local true solar time [LTST] as described in Section 2.1). An encounter with a convective vortex caused a sudden drop in the pressure and the convective cells led to quasi-periodic fluctuations of pressure with a period of about 100 s.

The topics related to PBL dynamics left out of the current study are detailed in the other papers of this issue: notable individual dust devil events (Lorenz et al., 2020), seismic signatures of vortices (Murdoch et al., in revision, Kenda et al., 2020), orbital observations of vortex tracks (Perrin et al., 2020), and aeolian science with InSight (Baker et al., 2020; Charalambous et al. in revision for this issue). As is shown in Banfield et al. (2020), InSight has a great potential too for studies of the nighttime, shear-driven turbulence associated with the nocturnal inversion. This topic is out of the scope of this study, which focuses on the daytime PBL dynamics, but will be developed in future papers.

2. Methods

2.1. InSight Observations

This study includes observations acquired in the first 400 sols of InSight operations at the surface of Mars. To indicate seasons on Mars, the Mars-Sun angle, referred to as the areocentric solar longitude L_s in degrees ($^\circ$), is used with the standard convention that 0° corresponds to northern spring equinox. InSight landing on November 26, 2018 corresponds to InSight sol 0 and $L_s = 295^\circ$ (northern late winter). The last sol considered in this study, sol 400, corresponds to $L_s = 134^\circ$ (northern midsummer). As far as the local time is concerned, in order to permit the analysis on seasonal timescales and the comparison of InSight observations with models, we use the sundial-equivalent Mars LTST in which noon corresponds precisely to the moment when the sun crosses the meridian.

The characteristics of the InSight instruments relevant for atmospheric science are summarized in Spiga et al. (2018) and in the Methods section of Banfield et al. (2020). The present study uses measurements from the pressure, temperature, and wind sensors onboard InSight, in addition to the magnetometer from the Auxiliary Payload Sensor Suite (APSS). Details of the calibration of the pressure sensor and the Temperature and Winds for InSight (TWINS) sensors can be found in Banfield et al. (2018). APSS measurements of pressure, wind, and temperature are continuously performed—except during brief, random anomalies of APSS electronics that cause measurements to stop during a couple of days, and the solar conjunction between sols 269 and 283 that prevented data transmission from Mars to Earth.

The InSight pressure measurements are routinely carried out at 10 Hz with a noise level of $10 \text{ mPa Hz}^{-1/2}$ from 0.1 to 1 Hz (typical noise at 1 Hz is thus of the order 10^{-2} Pa) rising to $50 \text{ mPa Hz}^{-1/2}$ at 0.01 Hz. Downlink limitations caused the InSight pressure data sets to be downsampled at 2 Hz in the sol intervals 14–167 and 262–269. This is significantly higher frequencies and lower noise levels than the previous pressure sensors sent to Mars (Martínez et al., 2017) and is appropriate to study expected daytime turbulent signatures: gusts, vortices, and cells (Spiga et al., 2018).

As is described in the Methods section of Banfield et al. (2020), the inclusion of an inlet tubing often does not prevent the pressure signal above 2 Hz to be correlated with wind speed—pointing toward either a loss of effectiveness of the pressure inlet, or mechanical or electrical noise in the pressure sensor. Thus, we consider herein only the pressure signal at frequencies $\leq 2 \text{ Hz}$: before our pressure drop search is performed, the signal is smoothed using a window of 0.5 s, that is, pressure is low-pass filtered with a 2-Hz cutoff. This is

appropriate for the search of vortex-induced pressure drops of duration above 1 s, which makes the majority of events according to existing studies, see, for example, Murphy et al. (2016).

The TWINS sensor booms are similar to those onboard the Curiosity rover (Gómez-Elvira et al., 2012). The booms are located on the InSight platform, facing outward in the opposite directions over the two solar panels. Their altitude from the surface is, respectively, 121.5 and 111.5 cm for the west and east booms (Banfield et al., 2020). Wind and air temperature are acquired at a frequency of 1 Hz and an accuracy of $\sim 1 \text{ ms}^{-1}$ for wind speed, 22.5° for wind direction, and 5 K for temperature. Owing to downlink limitations, the InSight TWINS data set is available with a frequency of 0.1 Hz on sol intervals 32–182 and 262–269; 0.5 Hz on sol intervals 14–30, 183–230, and 284–292; and 1 Hz on sol intervals 4–10, 231–261, and 293–400. The wind measurements are obtained from the TWINS booms' sensor acquisitions using look-up tables built on wind-tunnel calibration experiments and correcting from the influence of the lander platform elements using computational fluid dynamics simulations (Banfield et al., 2018). The measurements from the boom facing the prevailing wind are preferentially selected. In practice, the TWINS booms' wind measurements may be discarded because of sensor saturation (usually when wind speed is high, typically wind gusts $>20 \text{ ms}^{-1}$) and/or low Reynolds number (usually when wind speed is low, typically below 2.8 ms^{-1} ; see Banfield et al., 2020) and/or unfavorable wind direction (e.g., perpendicular to both booms). The actual frequency of TWINS wind and temperature measurements is thus typically 0.1–0.3 Hz.

The use of atmospheric temperatures retrieved by InSight deserves particular care. In daytime, the differences in air temperatures measured by the two booms can be large (Figure 2). In sustained wind conditions, thermal contamination by the lander elements (deck and solar panels) perturbs the air-temperature measurements of the TWINS boom facing the incoming ambient wind (Banfield et al., 2020). As is reported in Viúdez-Moreiras et al. (2020), during the dust storm from sol 40 to sol 60, temperature measurements by the west-facing boom are clearly anomalous; an increase in daytime air temperature is observed rather than the decrease expected in dustier conditions and correctly detected by the east-facing boom. This difference can be related to the southeasterly wind direction at that time: before the atmospheric flow reaches the west-facing boom, enhanced convective heat transfer between the lander and the boom causes the measured air temperature to be strongly overestimated by 15 K compared to the east-facing boom. A 10-K daytime excess in the temperature measurements of the west-facing boom, compared to the east-facing boom, is also found repeatedly from sol 160 to sol 400 characterized by steady southeasterly winds. This bias is stable in this 240-sol interval. In weak wind conditions (sols 60–160), the two TWINS booms yield consistent diagnostics for temperature, although with higher uncertainties associated with smaller Reynolds number (similarly to wind measurements, see Banfield et al., 2020). Discrepancies between the two booms' measured air temperature remain within the 5 K limit, which is the sensor uncertainty.

A strategy to mitigate those effects in the daytime is to consider, at each time, the minimum of the two temperature values deduced from each TWINS booms. In what follows, what is named “air temperature” and denoted T_a refers to this quantity. This is the simplest and most efficient method to date to select the boom performing the most reliable air-temperature measurements. In what follows, we use this TWINS air temperature mostly to compute the surface-to-atmosphere temperature gradient. Our conclusions still stand if another air-temperature estimate is considered (such as the maximum of the two temperatures from each of the booms, or an average of those temperatures, see Figure 8), since only the relative seasonal variations of atmospheric temperatures (and related quantities, such as surface-to-atmosphere temperature gradients) are analyzed.

Surface (i.e., ground) brightness temperature measurements are performed by the HP³ radiometer onboard the InSight lander. The details on this sensor calibration are described in Mueller et al. (2020). The HP³ radiometer sensors measure the surface brightness temperature in three spectral bands (8–14, 8–10, and 15–19 μm) at two different spots relative to the InSight lander, named the close spot and the far spot (Spohn et al., 2018). In what follows, we only use the surface brightness temperature retrieved in the far spot that, contrary to the close spot, is devoid of lander contamination (shadowing and thermal effects). The solar panel shadows pass through the near spot during the northern winter and can result in up to 20 K cooler temperatures in the afternoon and up to 10 K cooler daily average temperature. Considering the larger calibration uncertainties of the two spectral bands 8–10 and 15–19 μm (Mueller et al., 2020), in what follows surface brightness temperature is based on the sole 8–14 μm spectral band. Daytime conditions are the most

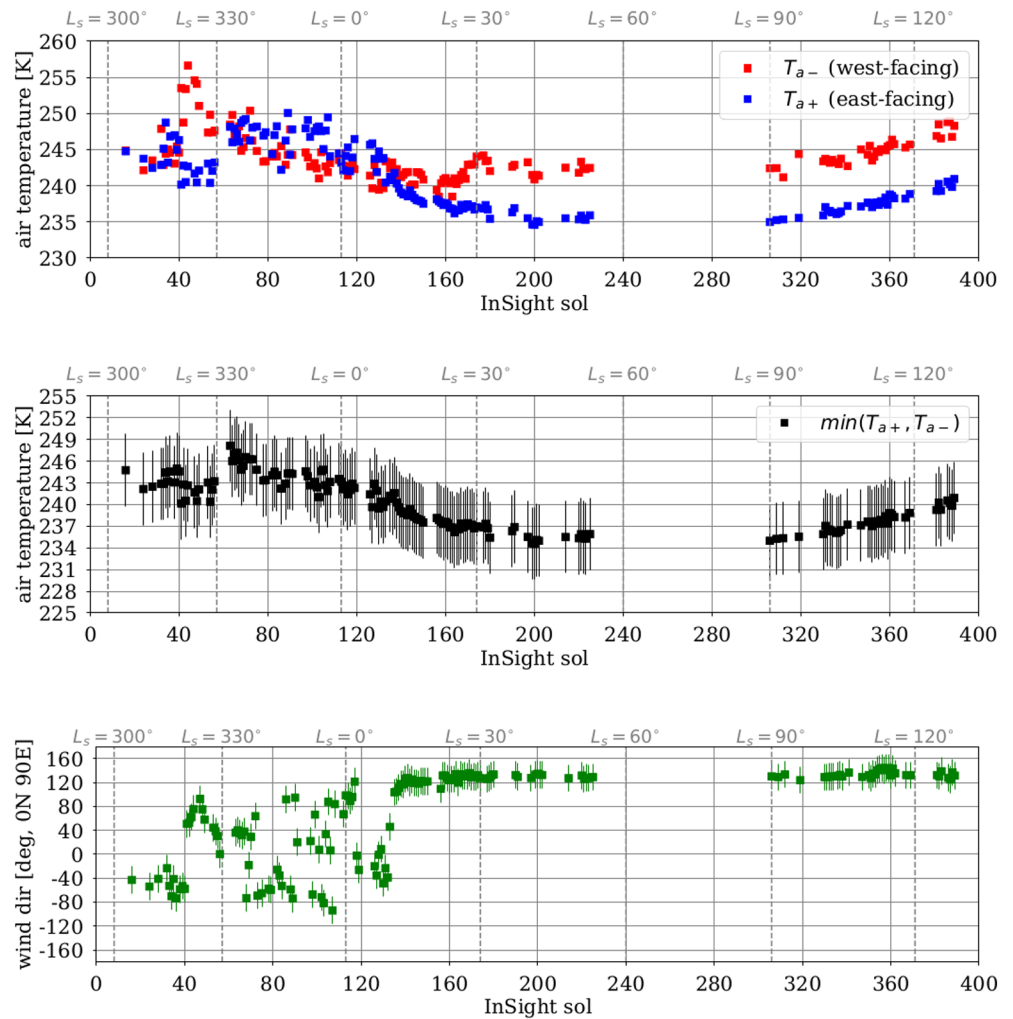


Figure 2. Typical measurements of temperature and winds for InSight air temperature (top panel for each separate boom, middle panel for air temperature estimated by taking the minimum value of both booms) and wind direction (bottom, obtained as indicated in the text) are shown for the first 400 sols of InSight operations. This figure is obtained with a similar methodology as what is described in greater detail in Figure 8.

favorable for surface temperature retrievals which uncertainty is better than 1.5 K between local times 10:00 and 15:30.

2.2. Vortex Detection Method

Convective vortices developing in the Martian PBL, and passing closely enough to the InSight lander, manifest as sudden pressure drops which amplitude ranges from 0.1 to 10 Pa and duration ranges from several seconds to several tens of seconds. This is the most distinctive signature of those vortices in the atmospheric sensors at the surface (see Murphy et al., 2016 for a review). Frequent—albeit not systematic—wind direction reversals are also associated with those encounters, as well as an increase of wind speed.

The method of detecting vortex pressure drops in the time series of InSight is slightly different than most published studies (e.g., Kahanpää et al., 2016). Those existing studies adopt a method detecting locally the drop of pressure from the ambient pressure measured just before the passage of a vortex. Here we adopt a method detecting globally pressure drops over the record of pressure of a full day. This simply appeared as more efficient and straightforward in the (unprecedentedly continuous) pressure records obtained onboard

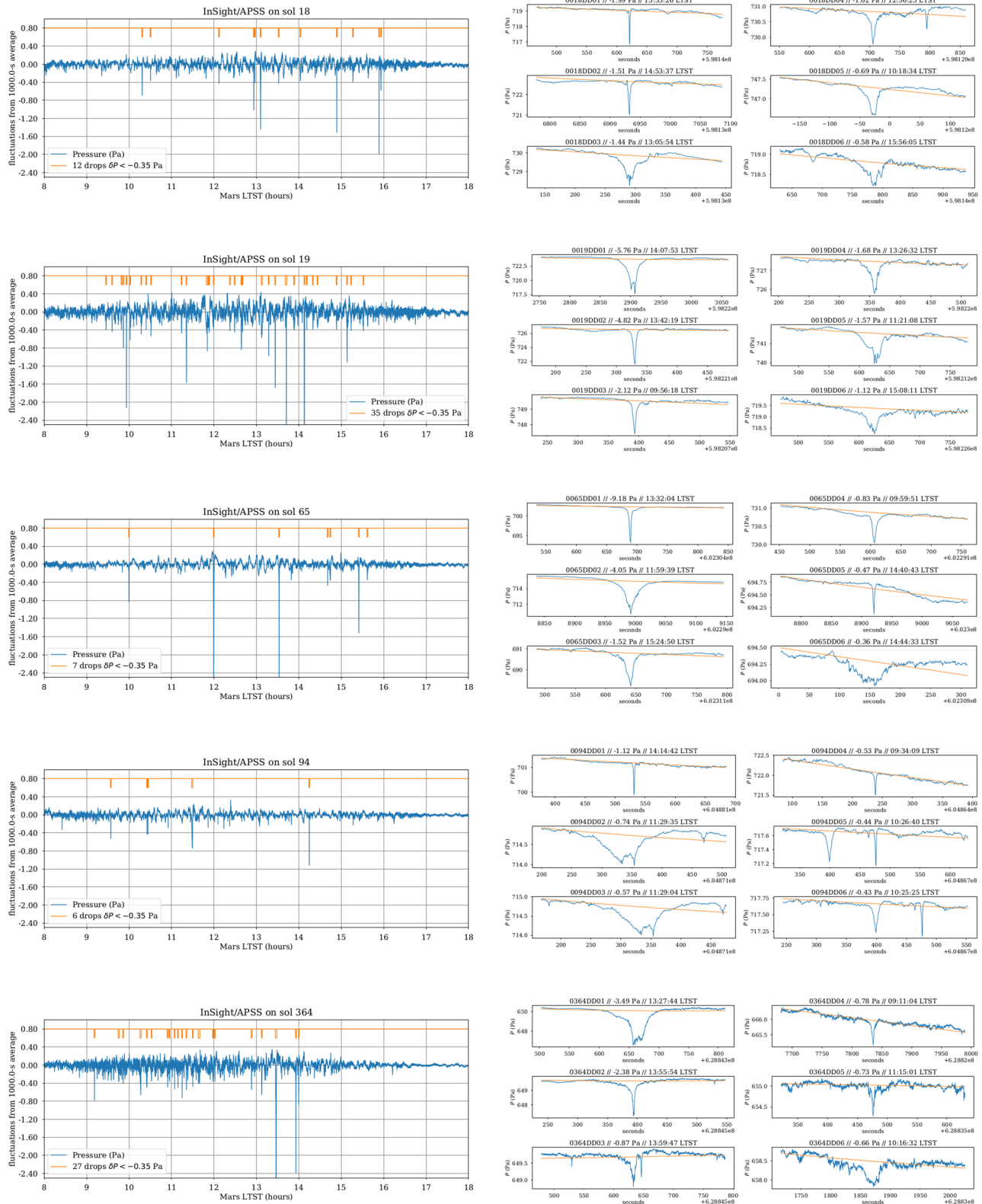


Figure 3. Typical examples of detecting vortex-induced pressure drops in the InSight time series are shown for sols 18, 19, 65, 94, and 364 (from top to bottom). The left plots show, in blue, the InSight daytime pressure measurements detrended by subtracting the signal smoothed with a 1,000-s Hanning window applied on the whole sol and, in orange, ticks for detected pressure drops. The right plots feature a subpanel plot for each of the deepest drops detected on each sol: the blue lines are the InSight pressure measurements and the orange lines are the smoothed signal.

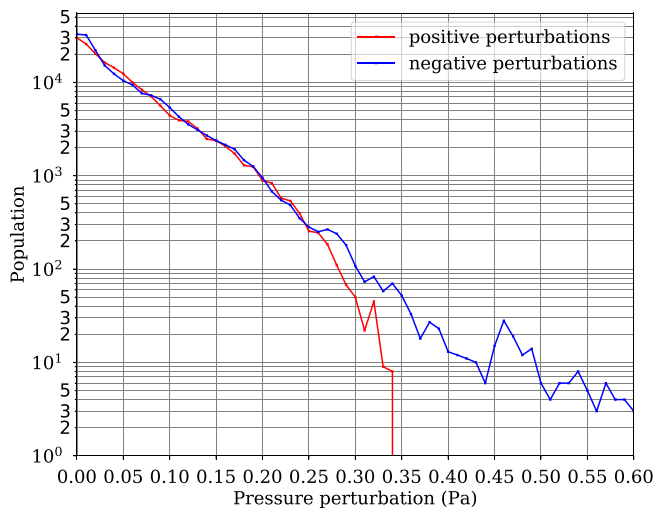


Figure 4. Histogram of absolute values of pressure perturbations from the 1,000-s smoothed signal, with positive perturbations in red and negative perturbations in blue. The analysis of sol 319 is shown as a typical example—a similar figure for other sols is obtained. The left part, where equivalent populations of positive and negative perturbations are found, corresponds to convective-cell-induced signatures. The right part, where only negative perturbations are found, corresponds to convective-vortex-induced signatures. The threshold adopted in the literature for vortex-induced detection on Mars is 0.3 Pa; we adopt here a more conservative estimate of 0.35 Pa.

vortex-induced pressure drops over cell-induced pressure lows is to select only pressure drops deeper than a certain threshold. A threshold value of -0.3 Pa is usually adopted (Ellehoj et al., 2010), although for pressure sensors with a higher noise level, a conservative -0.5 Pa limit is used (Kahanpää et al., 2016).

We can take advantage of the continuous InSight pressure data to discuss the choice of the threshold value for vortex detection in pressure time series. We examined the distribution of daytime pressure fluctuations from the 1,000-s window-smoothed signal, separating positive and negative perturbations (a typical example is shown in Figure 4). A good threshold to discriminate between convective cells and vortices corresponds to the value for which the distributions of positive and negative perturbations differ significantly, that is, negative pressure perturbations are more abundant than positive counterparts, hence cannot be attributed to convective cells. Figure 4 illustrates that the threshold value of -0.3 Pa employed in the literature is acceptable, yet adopting a threshold of -0.35 Pa is a more conservative choice for which pressure minimum can be more unambiguously attributed to convective vortices. We built two catalogs using the two distinct thresholds and found that the results discussed in this study on drop statistics and seasonal variability are not significantly altered by the choice of threshold. In what follows, results obtained with the most conservative catalog (using a -0.35 Pa threshold value) are shown.

Detrending with 500–2,000-s smoothing windows was tested and the 1,000-s window was finally selected as an optimum for vortex detection. A shorter window of 500-s tends to make vortex-induced pressure drops to become part of the smoothed signal and no longer considered as perturbations by the algorithm: as a result, long-lasting weak pressure drops are not detected and the other pressure drops are underestimated. We found that about 20% pressure drops detected with the 1,000-s window are left undetected with the 500-s window. A longer window of 2,000 s causes long-period fluctuations of pressure attributed to convective cells to be almost systematically included in the perturbation (detrended) signal rather than the smoothed signal; as a result, more than 30% of detected pressure drops are related to convective cells rather than convective vortices.

the InSight lander. We do not complement our vortex detection by analysis of the duration of vortex event—this is discussed in the study by Murdoch et al. (in revision). An example of five typical InSight sols with vortex detection using pressure time series is shown in Figure 3.

Our detection algorithm for vortex-induced pressure drop is set as follows. First, the InSight pressure signal over a complete sol is detrended from the diurnal cycle of pressure by subtracting a 1,000-s window average from the signal; then a search of the minima of pressure is performed between LTST 08:00 and 17:00 (which covers the local time of occurrence of drop events, see Section 3), starting from the deepest pressure drops and gradually removing the detected drops from the signal. This removal is realized on a window ± 30 s around the pressure local minimum, meaning that one limitation of the method is that double-dip pressure drops are counted as one event, unless the two local pressure minimum are occurring more than 60 s apart (as is the case for instance for sols 18 and 94 in Figure 3). Using a removal window ± 50 s rather than ± 30 s yields a population of detected pressure drops about 10% less abundant, yet similar results on statistics and seasonality.

How do we know that a detected pressure minimum corresponds to a convective vortex event? Compared to vortex-induced signatures, the variations of pressure associated with convective cells develop on longer timescales (several hundred seconds) and convective cells induce alternating pressure highs and lows, the cell-induced lows being less deep than the vortex-induced drops (Lorenz, 2012; Spiga, 2012). This distinction between daytime PBL vortices and cells is illustrated, for instance, in the observed pressure signal as shown in Figure 1 and the modeling results are shown in Figure 13. In the literature, a method to select vortex-induced pressure drops over cell-induced pressure lows is to select only pressure drops deeper than a certain threshold.

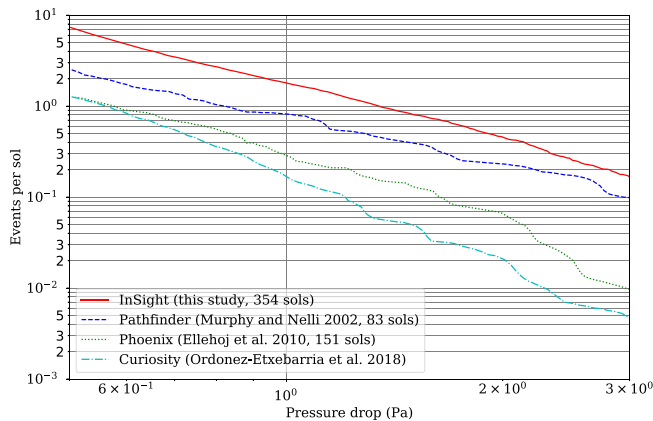


Figure 5. This logarithmic diagram shows the cumulative distribution of detected pressure drops per sol in the InSight time series (sols 0–400, from northern late winter $L_s = 295^\circ$ to midsummer $L_s = 134^\circ$), normalized by the total number of included sols. A total of 354 InSight sols, with uninterrupted pressure measurements in the daytime hours, are included to obtain the full red line, drawn with a bin size of 1.7×10^{-2} Pa. The equivalent statistics from other landers are included for the sake of comparison: Pathfinder (northern summer $L_s = 142^\circ$ – 183° at latitude 19°N) with the blue dashed line (Murphy & Nelli, 2002), Phoenix (northern spring and summer $L_s = 77^\circ$ – 148° at latitude 68°N) with the green dotted line (Ellehoj et al., 2010), and Curiosity (a full Martian year is included at latitude 4.6°S) with the cyan dash-dotted line (Ordonez-Etxebarria et al., 2018).

2.3. Large-Eddy Simulations

The results obtained from the InSight measurements are compared with turbulence-resolving LES. The principle of LES is to run a hydrodynamical solver of the Navier-Stokes equations at fine enough spatial resolution—on Mars, several tens of meters—to resolve the largest turbulent eddies in the daytime PBL, responsible for most of the transport of heat and momentum there (Michaels & Rafkin, 2004; Spiga et al., 2010; Toigo & Richardson, 2003). Such computationally expensive simulations are usually performed following the idealized setting of an infinite flat plain through doubly periodic boundary conditions. The turbulent eddies resolved by LES include the convective cells, gusts, and vortices developing in the daytime PBL—only the very-small-scale “local” turbulence is not resolved by LES.

Here we use the model described in Spiga and Forget (2009) and Spiga et al. (2010) which couples the Weather Research and Forecast hydrodynamical solver (Skamarock & Klemp, 2008), run at high spatial and temporal resolutions typical of LES (Moeng et al., 2007), to the physical parameterizations, notably radiative transfer, developed for Mars at the Laboratoire de Météorologie Dynamique (LMD; see e.g., Forget et al., 1999; Madeleine et al., 2011).

LES performed for this study dedicated to InSight extend those developed as pre-landing investigations in Kenda et al. (2017), Murdoch et al. (2017), and Spiga et al. (2018). The first two papers used LES with a resolution of 50 m and the third paper presented LES with a resolution of 10 m. Both are appropriate to resolve convective cells, provided the horizontal domain is sufficiently large to include several convective cells

so as to avoid boundary effects (Mason, 1989; Michaels & Rafkin, 2004). However, as far as vortices are concerned, the 50-m configuration only allows the largest vortices to be resolved and the 10-m configuration is too computationally expensive to be run on the whole local time period in which vortex activity takes place. Moreover, our objective in this study is to perform several LES runs in order to explore the sensitivity of vortex activity to local time, seasonal conditions, and ambient wind speed, which makes the 10-m-resolution approach untractable for this purpose.

We thus carry out in the present study LES with a spatial resolution of 25 m (using an integration time step of $1/4$ s), hence resolving vortices of diameters above 50 m. The horizontal domain extends over 481×481 grid points in the horizontal directions, which makes the total extent of the simulation domain 12×12 km. The top of the model is set at 10 km altitude (about twice the expected PBL depth) with 241 vertical levels. The surface temperature calculations in the model use a thermal inertia of $180 \text{ J m}^{-2} \text{ K}^{-1} \text{ s}^{-1/2}$ and an albedo of 0.16, corresponding to the conditions encountered at the InSight landing site, based on the HP³ radiometer far spot measurements considered to be representative of regional average conditions (Golombek et al., 2020). Radiative transfer computations assume the longitude and the latitude of the InSight landing site for the whole LES horizontal domain.

LES runs are initialized with a vertical temperature profile set to be uniformly similar at all model grid points and extracted at the relevant season and location from Global Climate Model (GCM) simulations (Forget et al., 1999; Millour et al., 2015). A random (noise) perturbation of 0.1-K amplitude is added to the initial temperature field to break its symmetry and help trigger convective motion. The LES integrations are started at 07:00 local time (LTST) and the diurnal evolution of incoming sunlight and temperature profile in the PBL are computed online during the LES integrations by the radiative transfer scheme (visible column dust opacity considered in the model is 0.8). A uniform and constant profile of ambient wind speed V (positive in the x direction) is prescribed in the model. Surface friction and turbulence alter this prescribed profile during the LES integrations, so that the value V of prescribed ambient wind represents wind conditions in the free atmosphere above the PBL; the value of ambient wind speed is about $V/2$ at the height relevant for InSight comparisons (1.165 m, see Section 2.1). The two values 10 and 20 ms^{-1} of ambient wind speed V

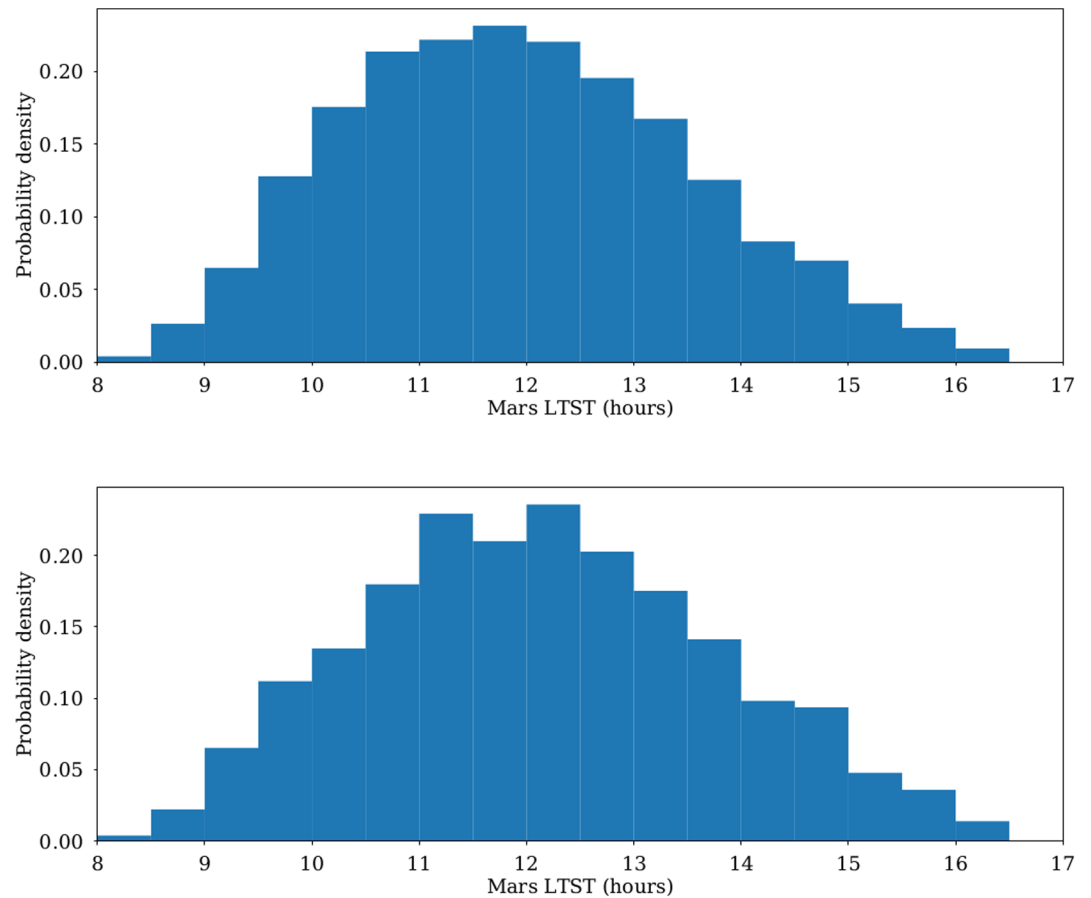


Figure 6. The vortex-induced pressure drops detected in the first 400 sols of InSight operations are gathered here in histogram plots with bins spanning half-an-hour intervals of local true solar time. The top plot includes all detected pressure drops (with a threshold of 0.35 Pa), while the bottom plot includes only the pressure drops deeper than 0.5 Pa.

prescribed in LES thus correspond to the near-surface ambient wind conditions encountered in the distinct sequences identified in Figure 8 and discussed in Section 4.1.

3. Vortex Population and Statistics

3.1. General Population

Convective vortices are known to be ubiquitous on Mars (Fenton et al., 2016), yet InSight appeared as a particularly active site for convective vortices. This has been demonstrated with 200 sols of observations by InSight in Banfield et al. (2020). Figure 5 confirms, after 400 sols of InSight observations, that the InSight lander operates in a location prone to numerous vortex encounters compared to previous missions equipped with a pressure sensor: Pathfinder (Murphy & Nelli, 2002), Phoenix (Ellehoj et al., 2010), and Curiosity (Kahanpää et al., 2016; Ordonez-Etxeberria et al., 2018). Considering the 1-Pa pressure drops as a proxy for the total number of vortex events per sol, the InSight lander experiences from northern late winter to mid-summer 10 times more convective vortices than the near-equatorial Curiosity lander did on average all year long and about twice as many as the tropical Pathfinder lander did in the northern summer season. This is all the more striking since, in the first 400 sols considered here for analysis, the annual peak of surface temperature has not been reached yet at the near-equatorial site of InSight (see Section 4.1).

A total of about 6,000 vortex-induced pressure drop events deeper than 0.35 Pa are detected between sols 0 and 400 of InSight operations. The strongest detected pressure drop is 9.2 Pa (Banfield et al., 2020; Lorenz et al., 2020), which is the deepest vortex-induced pressure drop detected to date on Mars. The sample of

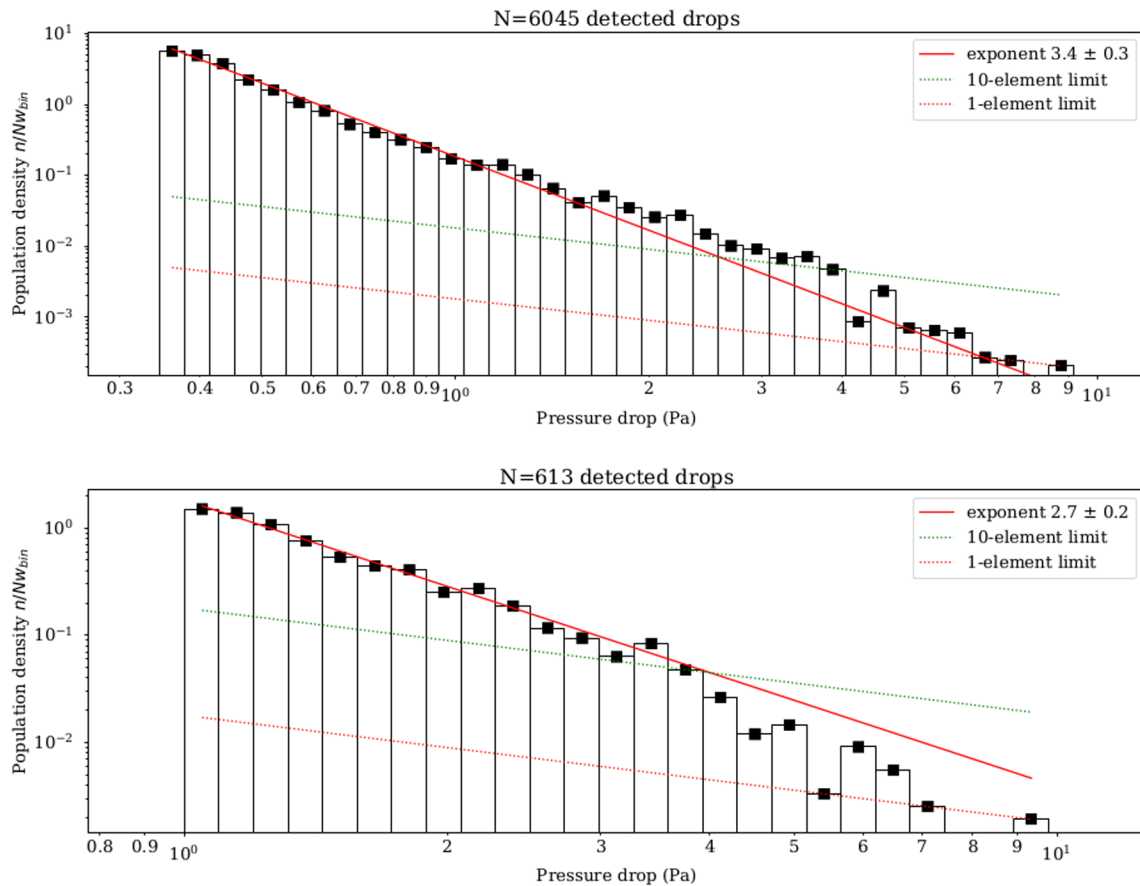


Figure 7. The population of detected pressure drops normalized by bin sizes (widths) is shown here on a logarithmic histogram with logarithmically scaled bin sizes, following, for example, Lorenz (2011). The top plot includes all vortex-induced pressure drops detected by InSight in the first 400 sols of operations. The bottom plot shows only vortices with pressure drops deeper than 1 Pa. An optimal power-law fit of the distribution, obtained by a nonlinear Levenberg-Marquardt least-squares approach, is shown as a red line with the optimum exponent shown in the legend. No error bars are included in the histograms when this power-law fit is performed; instead, the 3σ error on the power-law exponent (estimated from the covariance matrix) is indicated in the plot legend. The red and green dotted lines indicate the normalized population (value on the y -axis) corresponding to, respectively, 1 vortex and 10 vortices in each respective bins in the x -axis.

vortex detections shown in Figure 3 for five typical sols illustrates the strong diurnal, daily, and seasonal variabilities of detected vortex encounters at the InSight landing site.

3.2. Local Time

The local time of occurrence of convective vortices at the InSight landing site is between LTST 08:00 and 17:00 (Figure 6). The latest vortex-induced pressure drop deeper than 0.35 Pa detected at the InSight landing site in the first 400 sols of operations is at LTST 16:29. No detection prior to LTST 08:00 is obtained in the first 400 sols of InSight operations.

Overall, at the InSight landing site, the vortex activity is high between local times LTST 10:00 and 14:00. As is shown in Figure 6, the peak of activity for pressure drops is between 11:00 and 12:00 LTST, with an extent toward 12:30 for pressure drops stronger than 0.5 Pa. The mean of the distribution is found at, respectively, 11:57 and 12:09 LTST; the standard deviation of the two distributions shown in Figure 6 is 1.6 h. This is, apparently, an earlier peak than expected from studies based on missions other than InSight which exhibits a maximum occurrence of vortex-induced pressure drops around noon (Kahanpää et al., 2016; Murphy et al., 2016). However, Ordonez-Etxeberria et al. (2018) (their Figure 12) found that the distribution of daytime pressure drops detected by Curiosity peaked between 11:00 and 12:00 LTST when considering only local spring and summer, which are also the seasons covered by the present study addressing the first half a

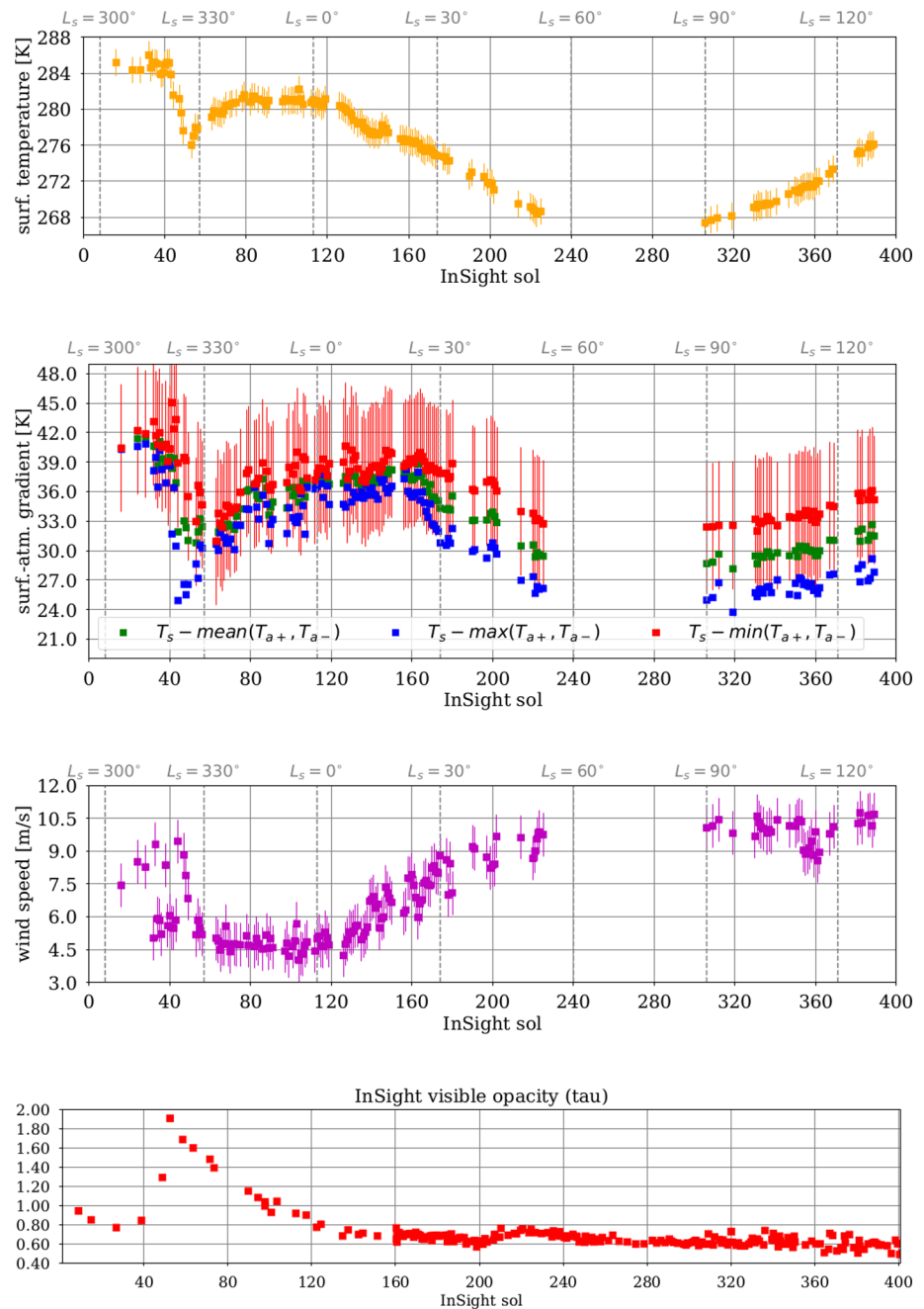


Figure 8. The seasonal evolution of daytime surface temperature (first panel from top), surface-to-atmosphere temperature gradient (second panel from top), and ambient wind speed (third panel from top) are shown for the first 400 sols of InSight operations. Each point is an average of the indicated quantity performed for each sol in the local time interval 11:00–14:00 (local true solar time). The uncertainties indicated in Section 2.1 are reported as error bars on the figures. Atmospheric wind and temperature measurements by Auxiliary Payload Sensor Suite/Temperature and Winds for INSight data are available for more sols than shown here; the three top diagrams only show the sols for which sufficient HP³ radiometer data for surface brightness temperature measurements were collected in the local time interval considered. The sky optical depth in the visible, obtained from InSight cameras (see Section 3.3.2 of Spiga et al. [2018] and Section 2.1 of Viúdez-Moreiras et al. [2020]), is shown in the bottom panel.

year of InSight operations. In the InSight data, there is also a tendency of the peak of vortex activity to occur earlier in the summer season, by about half-an-hour LTST. In local summer, Newman et al. (2019) found that the vortex encounters detected by Curiosity exhibited a double-peak structure at LTST 10:00–11:00 and 13:00–14:00 (see also simulations by Chapman et al., 2017). This double-peak structure is not found during the first northern summer season experienced by InSight.

3.3. Statistical Distribution of Pressure Drops

A question discussed at length in the existing literature (Jackson & Lorenz, 2015; Kurgansky, 2019; Lorenz, 2011) is whether the distribution of pressure drops caused by convective vortices (Figure 5) follows a power law or not, and what is the exponent of this power law. Clearly, the rich InSight data set permits the exploration of this question with an interesting new statistical perspective, given the large population of detected vortex events. The upper panel of Figure 7 shows a normalized log-log distribution (with logarithmic-sized bins) of all the vortices detected in the first 400 sols of InSight operations. A power-law distribution would appear as a linear trend in this diagram. Normalized distribution means that the number of events per bin is divided by the bin widths (Lorenz, 2011), which allows the differential distribution in pressure drops to be retrieved (Kahanpää et al., 2016).

The optimal fit we obtain in Figure 7 (upper panel), with a nonlinear Levenberg-Marquardt least-squares approach, suggests that the observed distribution of pressure drops at the InSight landing site is well represented by a power-law distribution with a 3.4 ± 0.3 exponent. The fit is particularly good for vortices having pressure drops between 0.3 and ~ 1.5 Pa. This is reasonably close to the exponent 3.7–3.8 found for Curiosity observations (Kurgansky, 2019; Steakley & Murphy, 2016) and to the exponent of 3–3.5 obtained from corrected Phoenix observations (Jackson et al., 2018). Here, we caution the reader that we did not attempt to perform a statistical analysis on the choice of function to fit the pressure-drop population. We adopted the power law as a means to compare the distributions obtained by InSight observations versus other measurements and numerical simulations, but our analysis does not rule out other possible functions to fit the distribution.

For pressure drops deeper than 1.5 Pa, the 3.4-exponent power law appears to underestimate the number of events actually detected by InSight. For that particular population, a power law with an exponent of 2.7 ± 0.2 provides a better fit, as is shown in the lower panel of Figure 7. We did not identify problems or biases in our detection method that would explain why the deepest pressure drops might be systematically overestimated, as would be implied by Figure 7 (top panel) if we assume that the 3.4-exponent power law is the reality. This power-law slope break might be due to the fact that the total number of the deepest detected drops is not sufficient to draw statistically meaningful conclusions about power-law exponents. This possibility is supported by the fact that the drop distribution did follow a 2.6-exponent power law when we considered the statistics of all pressure drops deeper than 0.3 Pa after only 40 sols of InSight operations.

4. Daytime Turbulence and Seasonal Variability Observed by InSight

4.1. Environmental Conditions and PBL Forcings

The seasonal evolution of the conditions relevant for turbulence in the daytime PBL is summarized in Figure 8.

Surface temperature T_s behaves as expected from the seasonal evolution at the equator, given InSight values of albedo and thermal inertia typical of Martian bare soil. A seasonal decrease of surface temperature is observed from northern winter ($L_s = 300^\circ$) to northern summer ($L_s = 90^\circ$), then surface temperatures rise again, pointing toward an expected seasonal peak at northern fall equinox ($L_s = 180^\circ$) as predicted, for example, from the Mars Climate Database (Millour et al., 2015). This behavior could appear as counterintuitive; however, the behavior of surface temperature observed at the InSight landing site in Figure 8 is explained by the near-equatorial position of the spacecraft.

A notable dip of daytime surface temperature—departing from the sine-shaped seasonal evolution—occurred from sol 40 to sol 80 and corresponds to a large regional dust storm outside the InSight landing site region that doubled the dust optical depth in the InSight landing site region (Banfield et al., 2020; Viúdez-Moreiras et al., 2020) (see Figure 8 lowermost panel). As a result, at the InSight landing site, the incom-

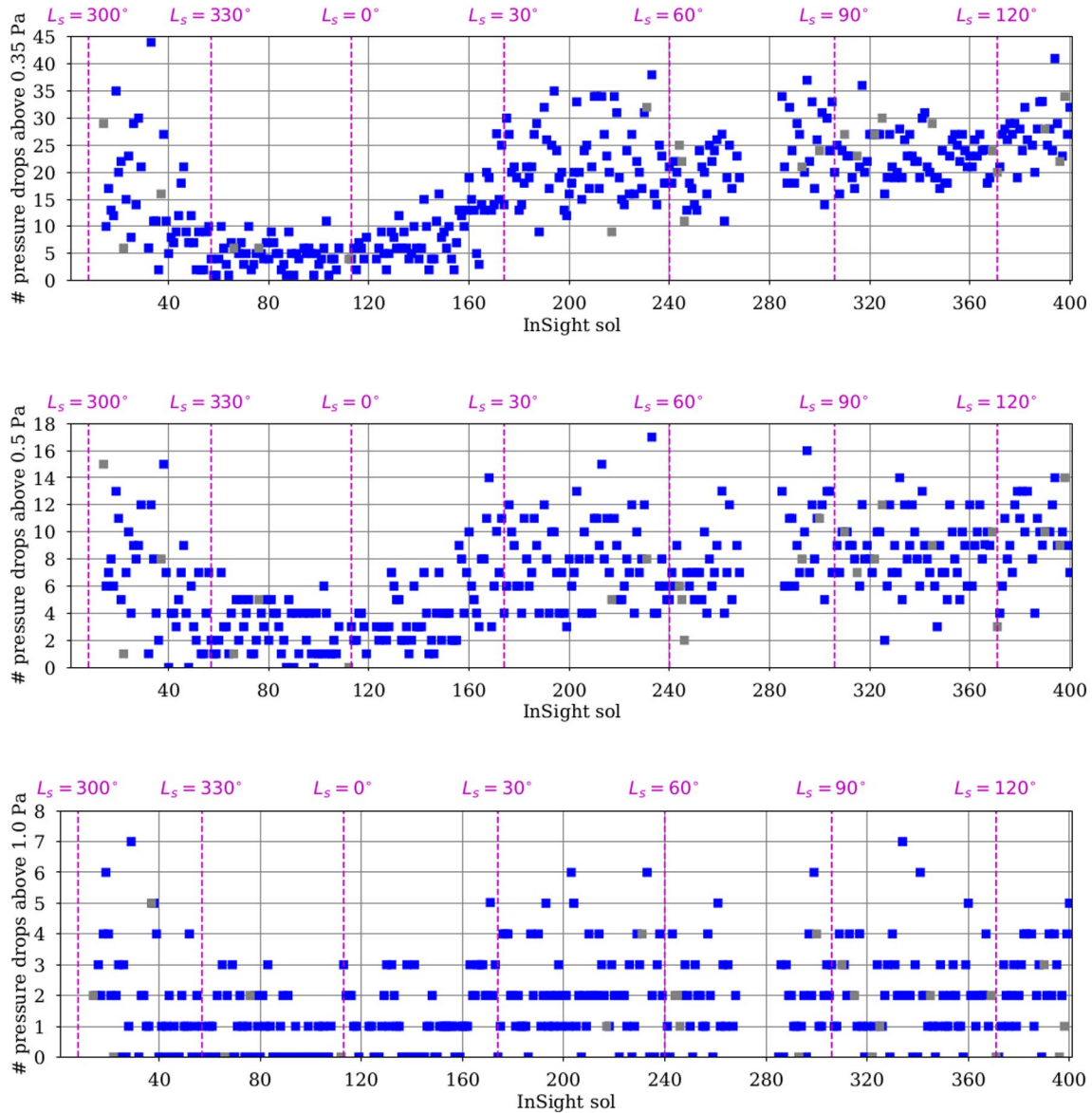


Figure 9. The number of vortex encounters detected in each sol of InSight operations is shown here for retrieved pressure drops above 0.3 Pa (top), 0.5 Pa (middle), and 1 Pa (bottom). The blue squares correspond to InSight sols with complete daytime coverage in the local time interval 08:00–17:00. The gray squares correspond to incomplete InSight sols, having gaps several hours long in the local time interval 08:00–17:00. In those particular cases, the number of vortex encounters is obtained by considering the number of detected pressure drops in the covered local times and correcting for local time gaps using a Gaussian diurnal distribution approximating the observed local-time distribution in Figure 6.

ing sunlight reaching the Martian surface is lower as a result of enhanced absorption and scattering by the additional dust particles present in the atmosphere, hence the dip in daytime surface temperature.

What drives PBL convection in daytime is the near-surface convective instability that we could diagnose by computing the surface-atmosphere gradient $T_s - T_a$. The seasonal evolution of this gradient follows to first order of the seasonal evolution of surface temperature; yet the impact of the local dust storm from sol 40 to sol 80 appears more prominent than it is on the surface temperature signal (Figure 8). The surface-atmosphere gradient also stays quite high on sol 150, while the surface temperature has started its seasonal decrease.

Another important control on PBL convection is the near-surface ambient wind speed V . Discussing the physical mechanisms underlying the seasonal evolution of large-scale wind speeds is out of the scope of this

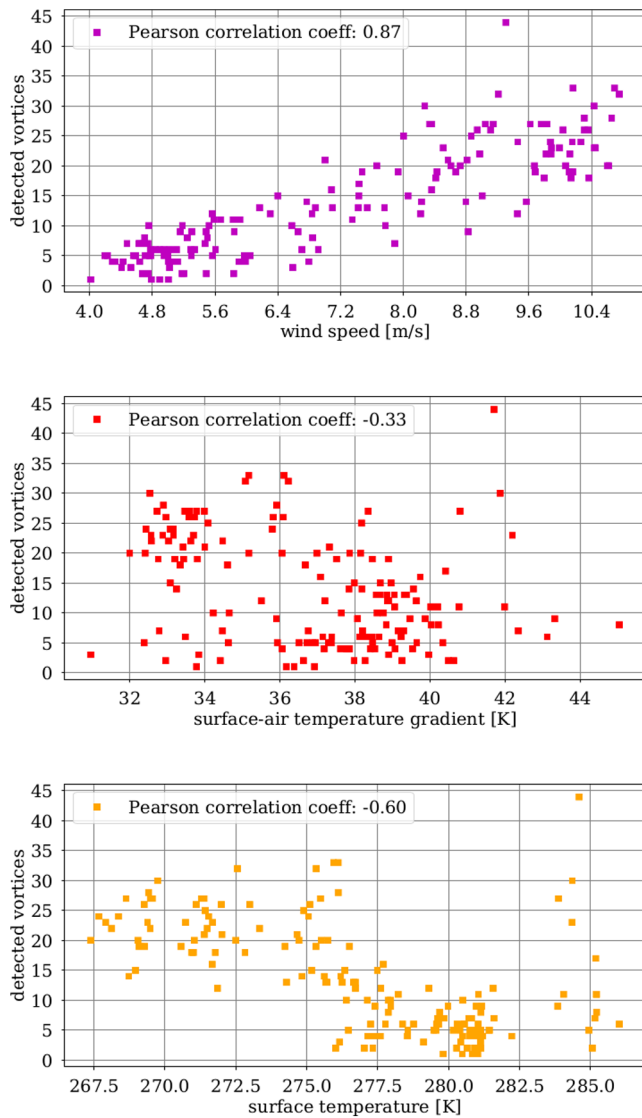


Figure 10. Counts of vortex-induced pressure drop are displayed as a function of environmental conditions (from top to bottom: wind speed, surface-to-atmosphere gradient, surface temperature). Each square represents a sol shown in Figure 9. The Pearson correlation coefficient is estimated in each case and indicated as a legend in each plot.

study (see Banfield et al., 2020; Spiga et al., 2018). Suffice to say here that the high daytime wind speeds in northern winter (beginning of the InSight mission, $L_s = 300^\circ - 330^\circ$) and northern spring to summer ($L_s = 60^\circ - 120^\circ$), and the decrease in late northern winter correspond to the transition between two annual wind regimes driven by a combination of large-scale (Hadley cells) and regional (western boundary currents) circulations.

From the seasonal evolution of surface-atmosphere temperature gradient and ambient wind speed, three sequences in the first half year of InSight can be drawn—the indicated season references the northern hemisphere:

1. *Early mission* (late northern winter, sols 0–40, $L_s = 300^\circ - 330^\circ$). This sequence is characterized by both high surface-atmosphere temperature gradient, mostly as a result of surface temperature being high, and high ambient wind speed in the northern winter “windy” season.
2. *Dust storm and spring* (early northern spring, sols 40–160, $L_s = 330^\circ - 30^\circ$). Following the rise of dust opacity at the InSight landing site caused by a regional dust storm that started on sol 40 (Banfield et al., 2020; Viúdez-Moreiras et al., this issue), both the surface-atmosphere temperature gradient and the ambient wind speed decrease. The decrease in surface-atmosphere temperature gradient is significant (from about 45 to 32 K) but, even in those regional dust storm conditions, near-surface temperature gradients on Mars remain super-adiabatic. The behavior of the wind speed is more subtle and less clearly related to the regional dust storm than temperature. Wind speed actually remains high at the beginning of the regional dust storm from sol 40 to sol 45. Then, the decrease in wind speed starting at sol 50 at $L_s = 326^\circ$ is predicted as a normal seasonal evolution by the pre-landing LMD GCM simulations in Spiga et al. (2018) even with no regional dust storm at this season (see their Figure 8). Indeed, the transition from northern winter solstice to spring equinox cause the wind speed to decrease, as a prelude to the seasonal reversal of the Hadley circulation closer to northern summer solstice. This difference of evolution between temperature and wind speed is also clear in the aftermath of the regional dust storm. When the dust opacity returns to levels seen at the beginning of the mission (around sol 100), both surface temperature and surface-atmosphere temperature gradient have risen again to close to pre-storm values, to follow the sine-shaped long-term seasonal variations; conversely, ambient wind speed remains low, in agreement with the seasonal evolution predicted by models (see Spiga et al., 2018 and also Baker et al., 2020).
3. *Aphelion season* (from northern mid-spring to summer, sols 160–400, $L_s = 30^\circ - 120^\circ$). Starting from sol 160, both the surface temperature and the surface-to-atmosphere temperature gradient decrease dramatically (-10 K), while at the same time, the ambient wind speed rises by almost a factor 2 to reach values slightly larger than in the *Early mission* sequence. This sequence is interesting for the seasonal evolution of turbulence, since it combines a wind speed equivalent to the *Early mission* sequence but surface temperature conditions 30 K colder than during this earlier sequence. Note that there is a gap in the range

$L_s = 60^\circ - 90^\circ$, due to a combination of HP³ radiometer troubleshooting and solar conjunction, but the pressure, temperature, and wind measurements available in this range shows that the atmospheric conditions are equivalent to those before and after the data gap.

4.2. Seasonal Evolution of Turbulence

4.2.1. Convective Vortices

Figure 9 shows the seasonal evolution of the number of convective-vortex pressure drops detected at the InSight landing site. In the literature, a quantity named the “Dust Devil Activity,” combining the sensible heat flux with PBL depth (Newman et al., 2017; Renno et al., 1998), is used to relate ambient conditions to vortex activity. It is difficult to use this diagnostic with InSight data since the PBL depth estimates are not robust enough (see Section 6) and, as is explained below, sensible heat flux is a degenerate diagnostic. We use instead more direct diagnostics to interpret the seasonal evolution of detected vortices: surface temperature, surface-to-atmosphere gradient, and ambient wind speed.

Figure 9 clearly indicates, over half a year of InSight observations, a much clearer correlation of the number of detected vortices with the ambient wind speed than with the surface-to-atmosphere gradient (or surface temperature)—whether the total population of vortices or the population of the deepest drop vortices are considered. The vortex activity at the InSight landing site is as intense in the *Aphelion season* sequence as in the *Early mission* sequence, despite a significant drop in surface-to-atmosphere gradient. In the *Dust storm and spring* sequence, the vortex activity also closely follows the evolution of ambient wind speed and, in the latest stages of this sequence, rises while the surface-to-atmosphere gradient is dropping significantly as a result of seasonal evolution. We note that the past studies also reported an increase in vortex detections in frontal conditions when the ambient wind speed was likely to be significantly higher (Ellehoj et al., 2010; Kahanpää et al., 2016; Steakley & Murphy, 2016). The strong correlation between InSight vortex detections and ambient wind speed is confirmed quantitatively in Figure 10: the Pearson correlation coefficient is close to 0.9 (positive linear correlation), while vortex detections are not correlated to surface-to-air temperature gradient, and weakly anti-correlated to surface temperature (at odds with physical expectations given the surface forcing of daytime PBL convection).

This correlation between the activity of convective vortices and ambient wind speed is degenerate. Higher ambient wind speed causes larger sensible heat flux, hence, a putatively more active turbulence—although on Mars the radiative forcing of the daytime PBL is dominant. However, vortices are also advected by the ambient wind (Balme et al., 2012; Reiss et al., 2014), hence, move faster if the ambient wind is large. Thus, if we assume a similar vortex formation rate at low and high wind conditions, the probability of encounter by a fixed station such as InSight would be larger in the high-wind case. LES are proposed in Section 5 to further investigate this question. At the same time, it should be noted that shearing may prevent the formation of convective vortices if the ambient wind speed is too high (Balme et al., 2012; Kurgansky et al., 2011). This does not seem to be the case at the InSight landing site where, even in the low-surface temperature and high-wind-speed conditions of the *Aphelion season* sequence, the number of vortex encounters is very high.

The seasonal variability of sensible heat flux H_s deserves further comments; this quantity can be calculated from InSight observations (Figure 11) using the bulk formulation $H_s = \rho c_p u_* \theta_*$, where friction velocity u_* and temperature scale θ_* are computed from Equations 3 and 4 in Spiga et al. (2018) using the InSight observations of, respectively, ambient wind speed V and surface-atmosphere gradient $T_s - T_a$, while atmospheric density ρ is computed from pressure P and air temperature T_a observed by InSight, and c_p is the specific heat capacity on Mars. Interestingly, as is shown in Figure 11, the seasonal variability of the number of vortex encounters at the InSight landing site is well correlated to the observed sensible heat flux. Drawing conclusions on the driving mechanisms for vortices from this correlation is tantalizing; we consider, however, that sensible heat flux is an ambiguous diagnostic for two reasons:

1. Contrary to Earth, in the low-density Martian atmosphere, the near-surface instability that drives the daytime turbulence is mostly a result of radiative warming through CO₂ (and, to lesser extent, H₂O and dust) absorption of incoming surface infrared flux (see Haberle et al., 1993; Sävijärvi, 1999; Spiga et al. 2010, Section 4). Sensible heat flux still plays a role in driving daytime turbulence on Mars, but less so than radiative contributions (see Section 4.2.2), in contrast to the terrestrial case. The contribution

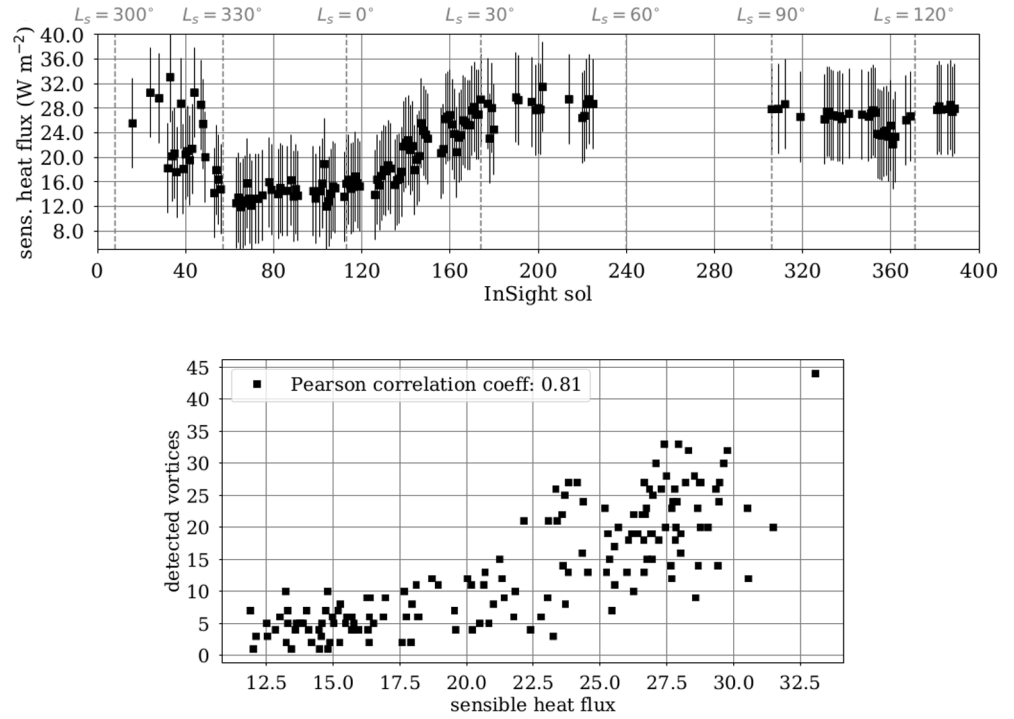


Figure 11. Sensible heat flux computed from InSight observations with a bulk formulation (see text) is shown in the top panel in a similar setting as Figure 8. Its correlation to the number of detected vortices is shown in the bottom panel in a similar setting as Figure 10.

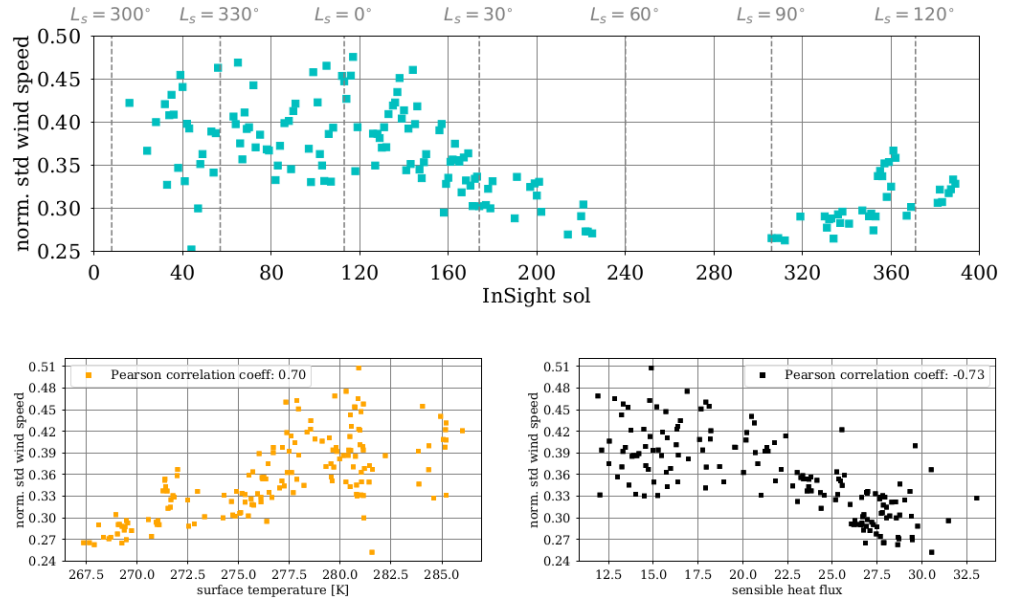


Figure 12. The seasonal evolution of normalized gustiness, defined as the standard deviation of wind speed (representing turbulence) normalized with the mean wind speed (i.e., the ambient wind speed), is shown here in the top plot in the same fashion as done in Figure 8). The same local-time interval of 11:00–14:00 as Figure 8 is used to compute the mean and standard deviation of wind speed. The correlation of normalized gustiness to surface temperature (bottom left panel) and sensible heat flux (bottom right panel) is shown in a similar setting as Figure 10. The correlation plot between normalized gustiness and wind speed is very similar to the bottom right panel (with a slightly different Pearson coefficient of -0.78).

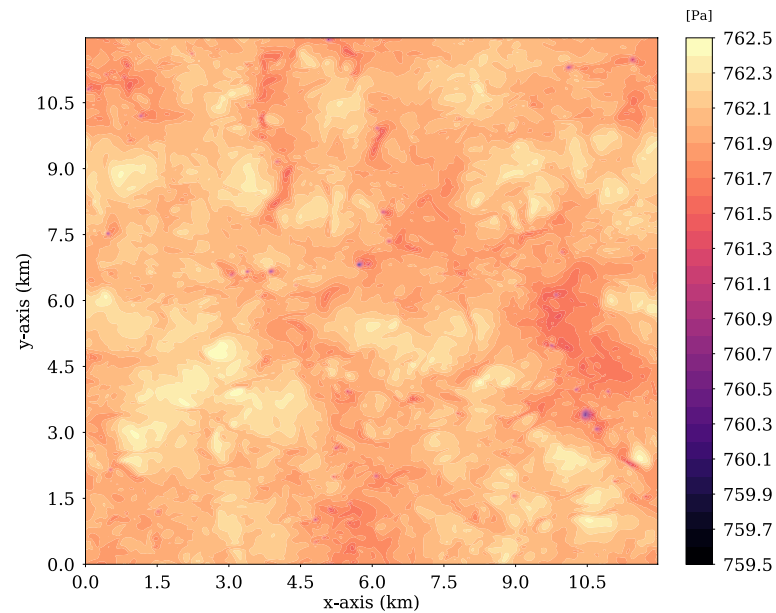


Figure 13. The typical surface pressure field obtained in our 25-m-resolution large-eddy simulations is displayed here on the whole 144 km² domain, for the case $L_s = 300^\circ$ with ambient wind $V = 10 \text{ ms}^{-1}$. The center of convective cells can be seen as large areas of “burgeoning” maxima of surface pressure in yellow colors. The convective vortices can be seen as localized round-shaped areas of pressure minima in violet colors.

of sensible heat flux on the Martian PBL only becomes dominant in extreme regional wind conditions encountered over steep slopes (Spiga et al., 2011).

2. Computing sensible heat flux mixes environmental variables controlling both the formation rate of vortices (e.g., near-surface instability) and the advection of vortices (e.g., ambient wind speed). Consequently, a valuable physical interpretation of the correlation between vortices and sensible heat flux is difficult.

4.2.2. Wind Gustiness

Figure 12 (top) shows the normalized daytime gustiness, obtained from the standard deviation of wind speed divided by the mean wind speed (computed over intervals of local times 11:00–14:00 LTST). Interestingly, in both the *Early mission* and the *Dust storm and spring* sequences, the gustiness remains roughly constant at values 35%–45%. There is no apparent influence of the local dust storm on this normalized gustiness: the strong decrease in vortex encounters noticed at sol 50 in Figure 9 is not observed in the normalized gustiness. Gustiness and vortices are two integral parts of daytime convective turbulence in the PBL; however, contrary to the vortex count, the local normalized gustiness is supposedly corrected of the effect of advection by the wind normalization (a vortex count normalized by ambient wind speed is sometimes used also; see Ellehoj et al., 2010 and Holstein-Rathlou et al., 2010). The fact that, in the *Dust storm and spring* sequence, vortex count decreases, while normalized gustiness does not, suggests that the advection effect is the dominant explanation for the seasonal correlation between vortex encounters and ambient wind speed at the InSight landing site.

What Figure 12 (top) also indicates is a decrease of gustiness in the *Aphelion season* sequence, from a value of 40% to 25%. This decrease of gustiness appears to be associated with the decrease of both the surface-to-atmosphere gradient and the surface temperature shown in Figure 8, while the ambient wind speed increases. However, the seasonal evolution puts the surface-to-atmosphere gradient at the same values at $L_s = 60^\circ$ as during the local dust storm at $L_s = 330^\circ$; this is not the case for surface temperature which reaches much lower values at $L_s = 60^\circ$. This, and the fact that normalized gustiness has not decreased during the local dust storm while it has decreased significantly at $L_s = 60^\circ$, indicates that normalized gustiness is primarily sensitive to surface temperature. Furthermore, Figure 12 (bottom) indicates a positive correlation (Pearson coefficient 0.7) between daytime gustiness and surface temperature, while a negative correlation

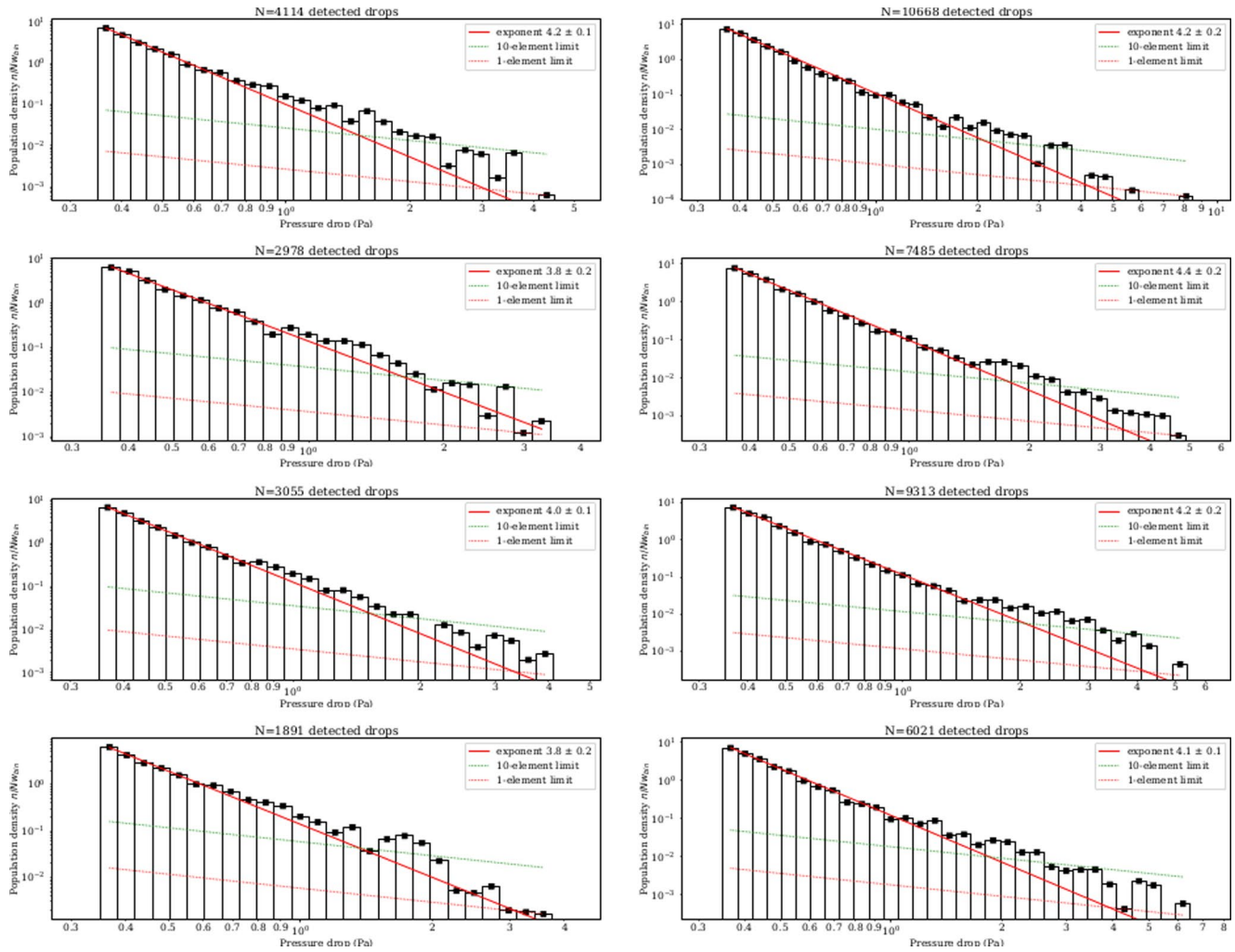


Figure 14. The normalized (differential) distributions of pressure drops deeper than 0.35 Pa detected in the large-eddy simulations are shown in similar diagrams to those shown in Figure 7. This is obtained by the same detection/histogram method as the one used for InSight observations. A total of 576-time series of pressure emulating different “sols” are included for each large-eddy simulations (LES) case. The left and right plots are obtained for, respectively, LES with ambient wind of 10 and 20 ms^{-1} , and rows from top to bottom correspond to simulations for $L_s = 300^\circ$, $L_s = 0^\circ$, $L_s = 30^\circ$, and $L_s = 120^\circ$. The number of vortex encounters detected in each case is indicated in the title of each plot.

is observed between daytime gustiness and sensible heat flux (or wind speed). This is in agreement with the Martian daytime PBL turbulence being mainly driven by radiative contributions rather than sensible heat flux, contrary to Earth—and further reinforces our claim in Section 4.2.1 that sensible heat flux could be well correlated to vortex encounters, without it being the actual driver of daytime turbulence on Mars. Lower daytime surface temperature in the *Aphelion season* sequence implies lower infrared flux from the surface to the atmosphere, hence lower radiative flux absorbed by the CO_2 atmosphere overlying the Martian surface, and as a result, less intense convective turbulence (Sävijarvi, 1999; Spiga et al., 2010). The *Aphelion season* sequence, during which gustiness is lower than in the *Early mission* sequence while vortex encounters are as numerous, strongly suggests that advection by ambient wind speed is a key element for explaining sequences of sustained vortex encounters at the InSight landing site.

The slight increase of normalized gustiness from 25% to 30% close to $L_s = 120^\circ$ is also correlated with the slow seasonal increase of surface temperature at the end of northerly summer. What remains to be explained is why the drop in daytime surface temperature during the regional dust storm is not associated with a drop of normalized gustiness. A possibility is that the dust particles injected by the distant regional dust storm and present in the PBL at the InSight landing site cause an increase of infrared absorption in the PBL that

Table 1

The Parameters Explored by the Eight Large-Eddy Simulations Carried out for This Study

Season L_s (°)	300	300	0	0	30	30	120	120
Ambient wind V (ms^{-1})	10	20	10	20	10	20	10	20

Note. Further details on the other (common) modeling settings are provided in Section 2.3. The ambient wind corresponds to conditions in the free atmosphere not influenced by friction and turbulence close to the surface; at the height of InSight measurements, the equivalent ambient wind is about $V/2$.

would add up to the CO_2 absorption and compensate (approximately) the decrease in energy input coming from the surface that received less sunlight because of dust absorption and scattering.

5. Comparison with Large-Eddy Simulations

We performed eight LES runs which all share the same simulation configuration described in Section 2.3. Table 1 summarizes the parameters chosen for the exploration of environmental conditions encountered at the InSight landing site during the first 400 sols of operation. What differs from one simulation to the other is the ambient wind speed, and the season considered for the LES radiative transfer computations (and, accordingly, the initial temperature profile). This is designed to explore the impact of the seasonal variations of environmental conditions described in Section 4.1. A typical pressure field predicted by LES is shown in Figure 13, with localized vortex-induced pressure drops forming at the intersection of larger scale convective cells (Kanak, 2006; Michaels & Rafkin, 2004; Spiga et al., 2016; Toigo & Richardson, 2003). It should be emphasized here that the results we discuss in this study with our 25-m LES will be in need to be confirmed by future work using higher resolution LES (typically 5 m, a factor of 5 better) to better resolve the population of small-radius vortices (Giersch et al., 2019; Nishizawa et al., 2016).

5.1. Vortex Statistics

To compare the vortex statistics predicted by our LES runs with those obtained from InSight observations (see Section 3), LES time series of pressure “measurements” emulating InSight’s are generated by randomly picking up a given grid point in the LES domain for each different sol (this is a practical application of the ergodic principle). We generate by this procedure 576 different “sols” for each LES listed in Table 1. Then, the exact same pressure-drop detection algorithm, as is used for the InSight data, described in Section 2.2, is applied to the LES time series for each generated “sol.”

The first result that can be discussed is the distribution of pressure drops obtained in the LES. As is shown in Figure 14, the differential distribution of pressure drops caused by convective vortices is suitably represented by power laws with exponents close to 4, which is in agreement with the results obtained with InSight (3.4 exponent; see Figure 7). We also note that, at all seasons, there is systematically about 2–3 times more vortex encounters in the case with higher ambient wind speed. The exponent of the optimum power-law distribution also appears to change with ambient wind speed (the larger the wind speed, the larger the exponent—further work on LES will be needed to confirm this point). How the power-law exponent changes with season is much less clear; no particularly clear trend can be drawn. We also note that the tendency found in InSight observations (Section 3.3) of the deepest pressure drops departing from a power law with exponents 3 and 4 appears to be reproduced by our LES runs. Future studies with a more extended period of time covered by InSight (e.g., two complete Martian years), thereby including more of the deepest vortex encounters, will allow this question to be fully addressed.

Figure 15 summarizes the emulated “daily” and seasonal variability of convective vortices obtained in LES. This figure is obtained by assembling the four LES cases corresponding to the seasons and the wind conditions experienced by InSight so far: high-wind cases for $L_s = 300^\circ$ (*Early mission* sequence), $L_s = 30^\circ$ (*early Aphelion season* sequence), $L_s = 120^\circ$ (*late Aphelion season* sequence), and low-wind case for $L_s = 0^\circ$ (*Dust storm and spring* sequence). A random selection among the 576 available “sols” for each considered case emulates the daily variability.

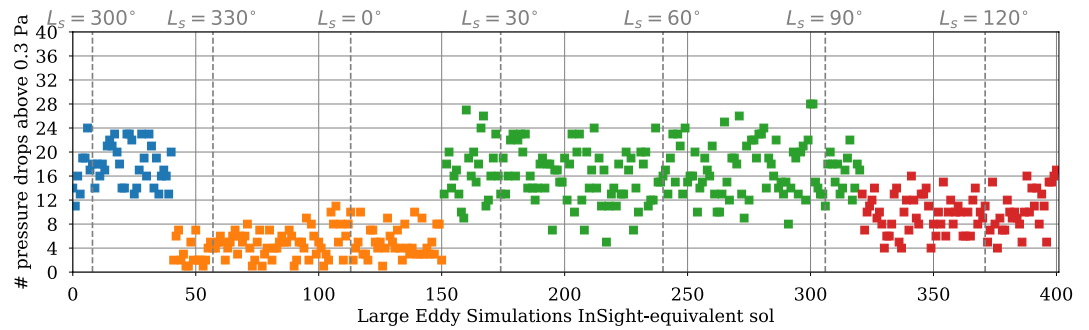


Figure 15. This seasonal plot emulates what is shown in Figure 9 about the seasonal evolution of InSight vortex encounters. Four large-eddy simulations (LES) cases corresponding to the seasons and the wind conditions experienced by InSight are included: $L_s = 300^\circ$ and $V = 20 \text{ ms}^{-1}$ (blue squares, Early mission sequence), $L_s = 0^\circ$ and $V = 10 \text{ ms}^{-1}$ (orange squares, Dust storm and spring sequence), $L_s = 30^\circ$ and $V = 20 \text{ ms}^{-1}$ (green squares, early Aphelion season sequence), $L_s = 120^\circ$ and $V = 20 \text{ ms}^{-1}$ (red squares, late Aphelion season sequence). A random selection among the 576 available “sols” for each considered LES case (i.e., color) emulates the daily variability.

The first remark is that, for all the cases displayed in Figure 15, the typical number of detected vortex encounters per sol is in agreement between the InSight observations and the LES. Second, the LES-reconstructed “daily” variability of vortex encounters within a given sequence can be quite large, as is observed by InSight. This shows that the daily variability of vortex encounters observed by InSight can be described in great part by the statistical nature of turbulence. Each sol of InSight observations would be an instance of InSight being placed at a different location in the horizontal structure of the PBL daytime turbulence (exhibited for instance in Figure 13). Third, the overall seasonal variability of convective vortices observed by InSight, and the three above-mentioned sequences, are well reproduced by the set of LES runs. A notable exception is the decrease of vortex encounters at $L_s = 120^\circ$ onwards, that is predicted by the LES but not observed by InSight (Figure 9).

5.2. Advection Effects

The results in Section 5.1 provide confidence that LES are a valuable tool to help to interpret the InSight vortex statistics. Can we confirm with LES the conclusion suggested in Section 4.2 that ambient wind speed seems to be a dominant driver of the seasonal variability of the number of vortex encounters? Figure 16 shows the LES-generated seasonal plot of vortex variability as in Figure 15, except that the LES runs are considered at the relevant seasons but with the choice of same ambient wind throughout (10 ms^{-1}). This figure demonstrates that, if not for the seasonal variability in ambient wind speed, the vortex encounter at the InSight landing should have decreased steadily, following the tendency of surface temperature (see Fig-

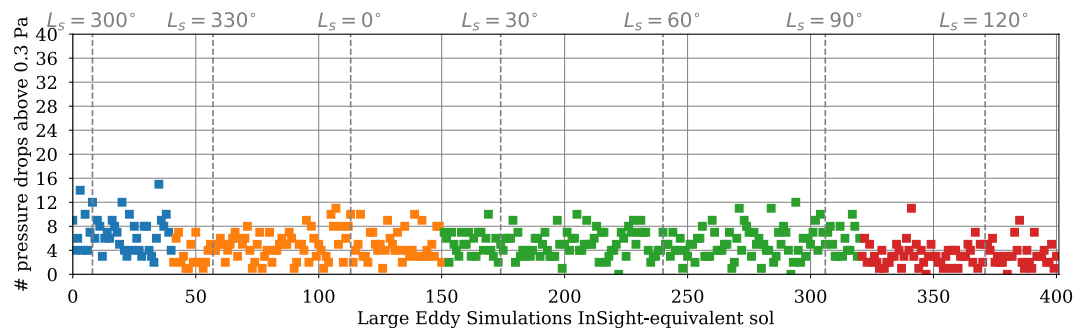


Figure 16. This figure is constructed similarly to Figure 15, except that only the large-eddy simulations cases with an ambient wind of 10 ms^{-1} are included: $L_s = 300^\circ$ and $V = 10 \text{ ms}^{-1}$ (blue squares, Early mission sequence), $L_s = 0^\circ$ and $V = 10 \text{ ms}^{-1}$ (orange squares, Dust storm and spring sequence), $L_s = 30^\circ$ and $V = 10 \text{ ms}^{-1}$ (green squares, early Aphelion season sequence), and $L_s = 120^\circ$ and $V = 10 \text{ ms}^{-1}$ (red squares, late Aphelion season sequence).

ure 8). This is a similar tendency as the one drawn for normalized gustiness in Section 4.2.2: the surface is colder and colder, meaning the surface infrared flux is lower and lower, thereby reducing the major energy input in the Martian PBL (i.e., absorption of surface infrared flux by CO₂ particles in the lowest part of the PBL), hence the strength of convective turbulent activity.

LES support the ambient wind speed as the major influence on the seasonal variability of vortex encounters observed at the InSight landing site. Now, as is discussed in Section 4.2, the influence of ambient wind speed might be two-fold. On the one hand, ambient wind speed influences vortex activity through the advection effect: stronger ambient wind advects more vortices to a given point, making the encounters on a given sol more frequent. On the other hand, ambient wind speed influences vortex activity through the formation rate: stronger wind on Mars could make the sensible heat flux term less negligible compared to the radiative term on the PBL energy budget, hence leading to stronger turbulence and more vortices forming—provided that enhanced shearing effects would not prevent the formation of vortices. We can use the LES to distinguish the two effects in a different fashion than what is permitted by the InSight time series. Instead of a vortex count performed along the time dimension to mimic InSight detections, we performed vortex counting on the whole horizontal LES domain of 144 km², identifying pressure minima in the complete pressure field as in Figure 13. This allows formation-rate effects to be emphasized, rather than advection effects.

The results are shown in Figure 17. We found that in our LES, for all the four seasons considered and consistently at all relevant local times, fewer convective vortices are forming when the background wind is doubled from 10 to 20 ms⁻¹. This could be considered as a counterintuitive result since large ambient wind speed enhances horizontal vorticity known to be a precursor of convective vortex formation (Rafkin et al., 2016; Toigo & Richardson, 2003). Yet, as is mentioned above in the text, this robust conclusion that less vortices form in larger ambient-wind LES runs could be explained by shearing effects: strong ambient wind is deforming the convective cells and adversely affecting the formation of vortices; in terrestrial field studies, windy days are well known to be met with far fewer, if any, dust-devil vortex encounters (Balme et al., 2012; Kurgansky et al., 2011; Lorenz et al., 2016). Another potential line of explanation is a possible lower longevity of convective vortices in the high-wind case—since vortices would be more short lived in the high-wind case, fewer of them would be detected in the horizontal LES pressure field. This was also found in the high-resolution terrestrial LES by Giersch et al. (2019): low-wind conditions favor more long-lasting vortices than high-wind conditions.

The analysis of LES thus strongly suggests that the seasonal variability of vortex encounters observed at the InSight landing site is dominated by the seasonal variability of wind speed, most probably through an advection effect.

5.3. Vortex Tracks

Although no visible dust devils have been detected by the InSight cameras (Banfield et al., 2020), numerous fresh tracks were detected from orbit in the region of the InSight landing site (Perrin et al., 2020), sometimes corresponding to tracks identified by InSight cameras (Banerdt et al. (2020) and Charalambous et al., in revision for this issue). Those dark tracks are putatively formed by convective vortices able to lift enough bright dust particles from the surface to make the underlying darker material apparent—although those vortices probably do not carry enough dust particles in their vortical structures to be seen as *dust devils* by the InSight cameras.

The formation of dark tracks seen from orbit can be emulated by LES. Assuming the above formation mechanism, tracks would correspond to locations where the wind stress would exceed a certain lifting/saltation threshold value (Michaels, 2006; see also Baker et al., 2020). We show in Figure 18 a possible mapping of tracks produced by our LES integrations, obtained by calculating the maximum of friction velocity (see Section 6.1 in Spiga et al., 2018) at each grid point during an active daytime 1-h interval of the LES simulation. The “contrast” of the image is set by defining the same color for all friction velocities below 1 ms⁻¹, this color acting as a proxy for undisturbed Martian soil devoid of dark tracks. The “equivalent orbital image” of dark tracks obtained from LES is then analyzed with the exact same semi-automated tracking procedure explained in Perrin et al. (2020).

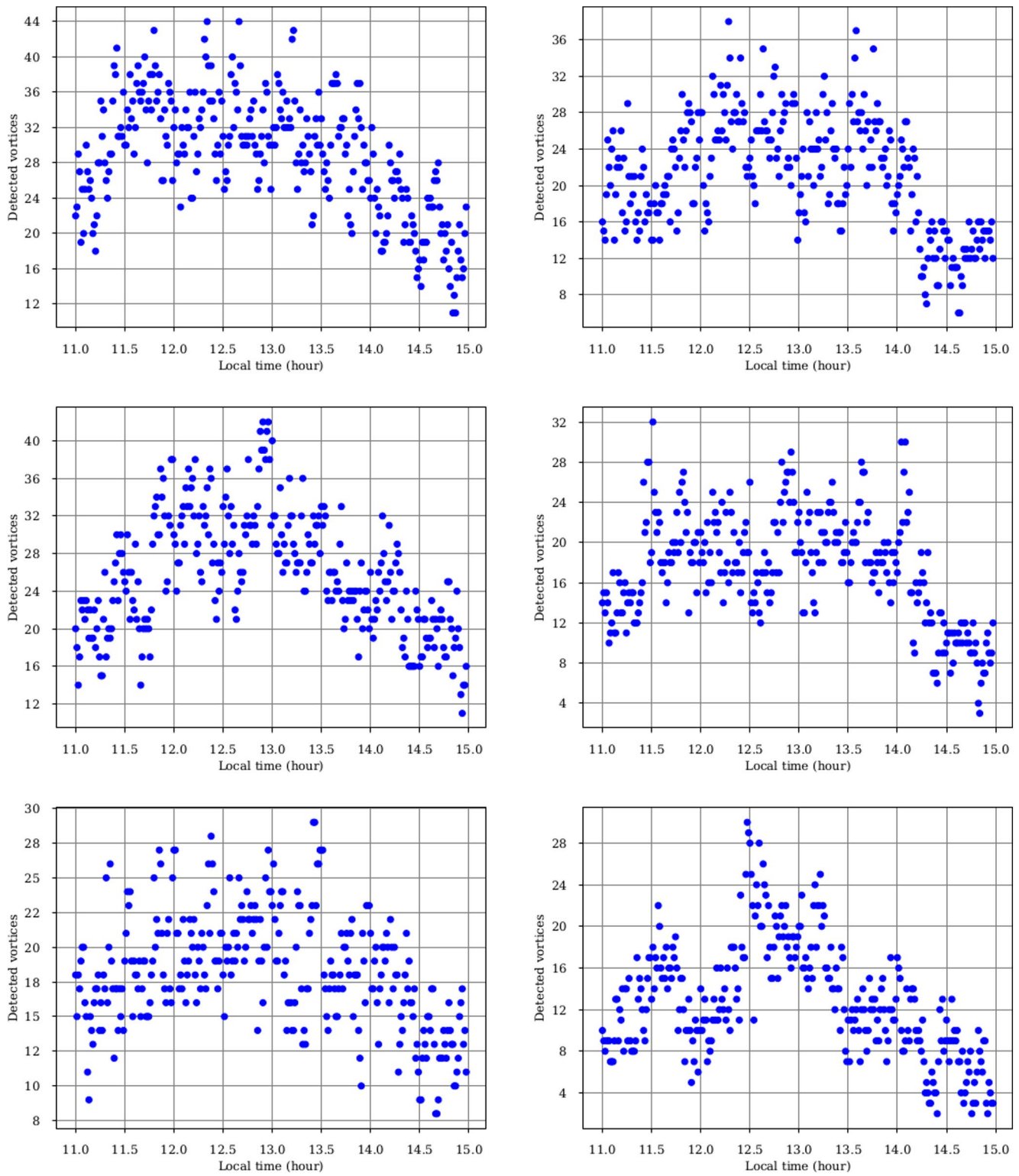


Figure 17. Pressure drops caused by convective vortices are detected here in the horizontal surface pressure field (as is shown in Figure 13) rather than InSight-equivalent time series. The plots show the number of vortices detected at different local times in the most active period for turbulence convection in large-eddy simulations (LES). The left and right plots, respectively, refer to LES runs with ambient wind speed of 10 and 20 ms^{-1} . From top to bottom, the LES cases for $L_s = 300^\circ$, $L_s = 30^\circ$, and $L_s = 120^\circ$ are considered.

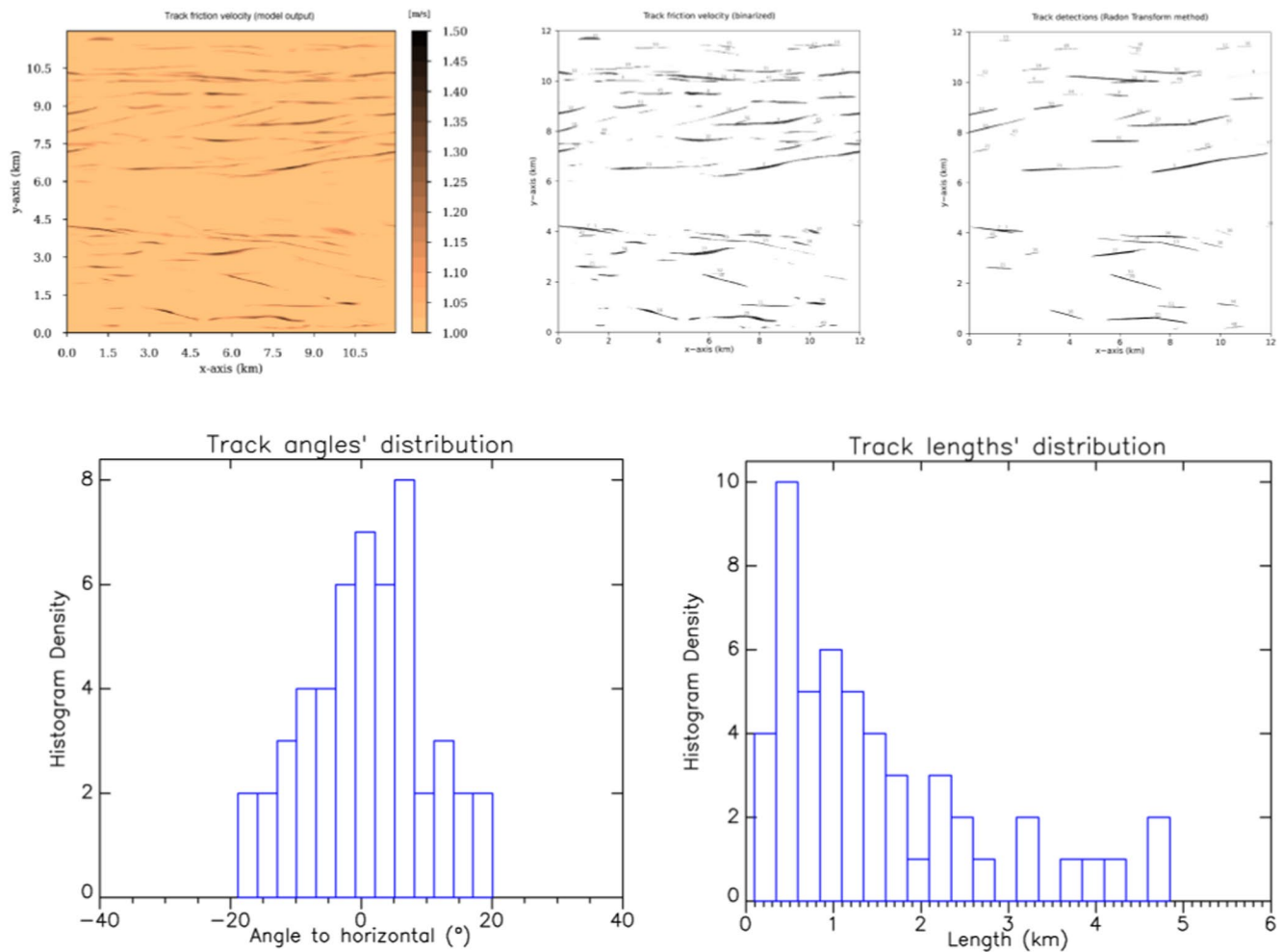


Figure 18. The upper left panel shows a “dark track” spatial map emulated from large-eddy simulations (LES) by extracting the maximum friction velocity at each grid point of the domain in the local time interval [12:00, 13:00]. The same orange color is used for all values of friction velocities below 1 ms^{-1} . Conditions for the Early mission sequence are considered here (i.e., LES run with $L_s = 300^\circ$ and ambient wind speed of 20 ms^{-1}). The upper middle and right panels, respectively, show a binarized version of the upper-left image derived from LES results and a Radon transform of this binarized image to detect linear tracks. Those detection methods used here on LES predictions are exactly similar to those developed for HiRISE images and detailed in Perrin et al. (2020). The histograms of the distribution of track angles (left) and lengths (right) are displayed at the bottom of the figure.

In Figure 18, a total of 51 tracks are detected on the 144 km^2 LES domain within 1 h. Considering 6 h of daytime vortex activity (Figure 6) and assuming for simplicity a constant formation rate, this translates to a maximum track formation rate of $2 \text{ tracks/sol/km}^2$. This is clearly much larger than the minimum formation rate of $0.04\text{--}0.06 \text{ tracks per sol per km}^2$ found by Perrin et al. (2020), even considering the very exceptional period of intense dust devil activity at the beginning of the InSight mission (i.e., $0.68 \text{ tracks/sol/km}^2$). Actually, this “threshold” value of 1 ms^{-1} is chosen to be permissive to detect enough tracks to form a reasonable statistics to compare to images in Perrin et al. (2020) in the next paragraph. A normal track formation rate, like in Perrin et al. (2020) and the pre-landing estimates by Reiss and Lorenz (2016), yields about 1 track/h for an LES domain size of 144 km^2 . This means that only the darkest track in Figure 18, obtained for friction velocities of about $1.4\text{--}1.5 \text{ ms}^{-1}$ (200 values among the 8×10^8 values output by LES over the considered hour), would correspond to a realistic case of the orbital images of Perrin et al. (2020), which illustrates the stringent conditions for lifting dust particles from the surface in the vicinity of the InSight landing site. This is echoed by the scarcity of surface change events witnessed by InSight cameras, which corresponds to the strongest pressure drops and associated wind gusts monitored by InSight APSS (see Baker et al., 2020 and Charalambous et al. in revision for this issue).

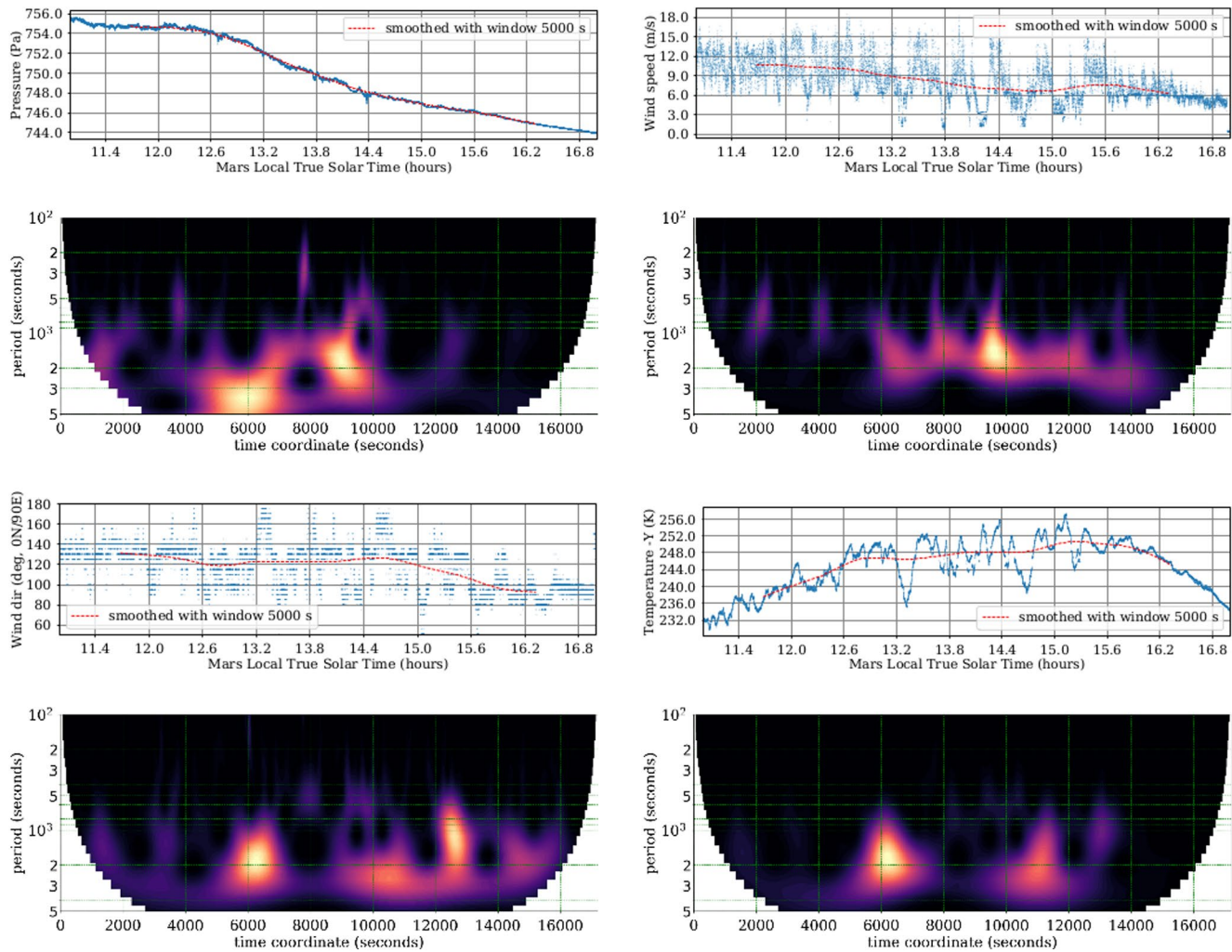


Figure 19. In this figure, the blue lines show the observed daytime signal by the InSight Auxiliary Payload Sensor Suite instruments on sol 234 ($L_s = 57^\circ$): pressure (upper left), wind speed (upper right), wind direction (lower left), and air temperature (lower right). The red lines in each subpanel correspond to a smoothing average of the signal with a Hanning window of 5,000 s. The signal detrended by this smoothing average is analyzed with wavelet transforms to identify quasi-periodic patterns. Each displayed atmospheric time series has its wavelet analysis shown below the line plot and encompassing the same local time interval. Details on the wavelet analysis are provided in the Methods section of Banfield et al. (2020). It is based on the approach described in Torrence and Compo (1998) and coded in Python by Evgeniya Predybaylo.

The typical track length (ranging from 500 m to about 5 km) and the distribution angle (ranging 20° apart from the ambient wind direction, with a standard deviation of 9°) are in good agreement with the values obtained with HiRISE orbital images with the same method (Perrin et al., 2020). Furthermore, the low-standard deviation of tracks under fairly high ambient wind speed (10 ms^{-1}) confirm that the linearity of tracks increases with the ambient wind speed (see Balme et al., 2012 and Perrin et al., 2020 on Earth and on Mars, respectively).

6. Convective Cells and an Estimate of the Convective PBL Depth

The pressure sensor on board InSight is more sensitive than any pressure sensor sent on a lander to Mars (Banfield et al., 2018). This allows the signal of convective cells to be detected as quasi-periodic signals in the pressure time series, on longer timescales than vortices and gusts (see Figure 1) because their spatial scales are larger (see the brightest areas in Figure 13). Here we report the first analysis on a typical case, but a more in-depth analysis is warranted in the future.

A particularly clear example is provided in Figure 19. On all atmospheric measurements (pressure, wind speed, wind direction, and atmospheric temperature), quasi-periodic variations with periods 1,500–2,000 s are observed (a similar signal is also found on the solar array data, see Lorenz et al., 2020). This is also observed in the field on Earth (Lorenz, 2012) and predicted by LES (Spiga, 2012; Spiga et al., 2018).

Quasi-periodic variations of pressure, wind, and temperature are caused by the advection of convective cells by the ambient wind. In other words, this signal in the InSight data is another illustration of the key role played by advection of PBL turbulent structures by the ambient wind. The width of convective cells scales with the PBL mixing height (Willis and Deardorff, 1979 found the former is a factor 1.2 of the latter); hence, the quasi-periodic signal makes it possible to estimate the PBL mixing height.

In the case considered in Figure 19, the ambient wind is about $7\text{--}8\text{ ms}^{-1}$ when the quasi-periodic oscillations appear, which means the width of the convective cells (hence, the PBL depth) ranges from 10.5 to 16 km, assuming direct advection of the cell-induced pressure signatures by the ambient wind speed. It is important to note here that, in an LES case where the PBL depth is known, Spiga (2012) found that multiplying the quasi-period with the ambient wind yields an estimate of PBL depth that is about twice the real value of the PBL depth deduced from studying the vertical mixing depth in LES (e.g., Spiga et al., 2010). We conclude that the PBL depth in the case of the InSight observations ranges from 5 to 8 km, which is typical of active Martian daytime PBL conditions (Fenton & Lorenz, 2015; Hinson et al., 2008; Tillman et al., 1994). However, this range is also large and corresponds to the typical regional variability of the PBL depth on Mars (Hinson et al., 2008, 2019; Spiga et al., 2010). Furthermore, the typical PBL depth obtained for the LES with InSight conditions is about 5–6 km, that is, corresponding to the lower range obtained by the above estimate.

This makes the estimate of PBL depth by the quasi-periodic signal probably valid only to an order of magnitude. As a result, by this method, it was difficult to obtain the variability of the PBL depth with local time and season. Furthermore, the case displayed in Figure 19 is one of the most favorable: while quasi-periodic signals are very often detected in the daytime measurements by InSight, clearly determining their period has resulted to be challenging—especially given the challenges posed by InSight temperature measurements (see Section 2.1). A systematic exploration is warranted as future work and considered out of the scope of this study.

7. Conclusions

The conclusions of our study may be summarized as follows:

1. High-sensitivity continuous pressure, wind, and temperature measurements by InSight exhibit signatures of gusts, convective cells, and vortices, associated with daytime PBL turbulence. InSight measurements can be fruitfully compared to turbulence-resolving LES.
2. Simultaneous quasi-periodic variations of pressure, temperature, and winds, with periods 1,000–2,000 s, are attributed to the advection of convective cells by the ambient wind. The typical daytime PBL mixing height obtained from this signal is in the range 5–8 km.
3. The InSight landing site is particularly prone to vortex encounters. More than 6,000 pressure drops deeper than 0.35 Pa are detected in the first 400 sols of InSight operations.
4. The differential distribution of observed vortex-induced pressure drops at the InSight landing can be well represented by a power law with a 3.4 ± 0.3 exponent, although the power-law fit for the vortices with the deepest pressure drops appears to differ from this whole-population fit.
5. The equivalent distribution in LES is close to InSight observations, exhibiting exponents around 4.
6. With the help of LES, the variability of vortex encounters from one sol to the other at the InSight landing site can be explained in great part by the statistical nature of daytime PBL turbulence.
7. On a seasonal basis, the vortex encounters at the InSight landing site are much more correlated to the ambient wind speed than with the surface temperature and surface-to-atmosphere temperature gradients. This conclusion is supported by LES.
8. Normalized wind gustiness (i.e., standard deviation of wind speed over mean wind speed) is positively correlated to surface temperature rather than sensible heat flux, confirming the radiative control of the daytime Martian PBL.

9. An analysis of vortex population in the horizontal pressure field of the LES runs indicates that fewer convective vortices are forming when the background wind is doubled from 10 to 20 ms⁻¹.
10. Conclusions 7–9 led us to conclude that the long-term seasonal variability of vortex encounters at the InSight landing site is mainly controlled by the advection of convective vortices by the ambient wind speed.
11. Typical tracks followed by vortices forming in the LES show a similar distribution in direction and length as orbital imagery of the InSight region; to match the rate of track formation, only the strongest vortex-induced wind gusts predicted by LES (close to friction velocities 1.5 ms⁻¹) has to lead to bright dust particles being moved on the surface.

The meteorological measurements by the instruments on board InSight make a unique rich data set to study the daytime PBL dynamics, as is already demonstrated by the first 400 sols of InSight operations. It is not possible to fully unleash here, in one study, the potential of the InSight measurements to study atmospheric turbulence. Some conclusions reached in this study will have to be revisited once a more extended period of time has been monitored by InSight (covering in particular northern fall, the season at which the annual maximum of surface temperature is reached at the near-equator landing site of InSight). We also emphasize here that further comparisons between turbulence-resolving models and in situ high-frequency continuous measurements at the surface of Mars will allow the broadening of knowledge on PBL turbulence both on Mars and elsewhere.

Data Availability Statement

The datasets produced to obtain the figures in this study, along with the Python codes used for the data analysis, are available in the citable online archive <https://doi.org/10.14768/2ddaba56-cf61-4d5b-83b7-e4a079ed836b> hosted at the Institut Pierre-Simon Laplace (IPSL) datacenter (Spiga, 2020). All InSight data used in this study are publicly available in the Planetary Data System. Data from the APSS pressure sensor and the temperature and wind (TWINS) sensor referenced in this study is publicly available from the PDS (Planetary Data System) Atmospheres node. The direct link to the InSight data archive at the PDS Atmospheres node is: https://atmos.nmsu.edu/data_and_services/atmospheres_data/INSIGHT/insight.html. Surface brightness temperature measured by the HP³ radiometer is publicly available from the PDS Geosciences node: <https://pds-geosciences.wustl.edu/missions/insight/hp3rad.htm> (DOI reference <https://doi.org/10.17189/1517568>). The code for the Large-Eddy Simulations carried out for this study is managed on an online repository at LMD (access granted upon request); this study uses the revision 1937 of the code. This study is InSight Contribution Number 115.

References

- Baker, M., Newman, C., Charalambous, C., Golombek, M., Spiga, A., Banfield, D., et al. (2020). Vortex-dominated aeolian activity at InSight's landing site, Part 2: local meteorology, transport dynamics, and model analysis. *Journal of Geophysical Research: Planets*, 121, e2020JE006514. <https://doi.org/10.1029/2020JE006514>
- Balme, M. R., Pathare, A. V., Metzger, S. M., Townner, M. C., Lewis, S. R., Spiga, A., et al. (2012). Field measurements of horizontal forward motion velocities of terrestrial dust devils: Towards a proxy for ambient winds on Mars and Earth. *Icarus*, 221(2), 632–645. <https://doi.org/10.1016/j.icarus.2012.08.021>
- Banerdt, W. B., Smrekar, S. E., Banfield, D., Giardini, D., Golombek, M., Johnson, C. L., et al. (2020). Initial results from the InSight mission on Mars. *Nature Geoscience*, 13(3), 183–189. <https://doi.org/10.1038/s41561-020-0544-y>
- Banfield, D., Rodriguez-Manfredi, J. A., Russell, C. T., Rowe, K. M., Leneman, D., Lai, H. R., et al. (2018). InSight Auxiliary Payload Sensor Suite (APSS). *Space Science Reviews*, 215(1), 4. <https://doi.org/10.1007/s11214-018-0570-x>
- Banfield, D., Spiga, A., Newman, C., Forget, F., Lemmon, M., Lorentz, R., et al. (2020). The atmosphere of Mars as observed by InSight. *Nature Geoscience*, 13, 190–198. <https://doi.org/10.1038/s41561-020-0534-0>
- Chapman, R. M., Lewis, S. R., Balme, M., & Steele, L. J. (2017). Diurnal variation in Martian dust devil activity. *Icarus*, 292, 154–167. <https://doi.org/10.1016/j.icarus.2017.01.003>
- Ellehoj, M. D., Gunnlaugsson, H. P., Taylor, P. A., Kahanpää, H., Bean, K. M., Cantor, B. A., et al. (2010). Convective vortices and dust devils at the Phoenix Mars mission landing site. *Journal of Geophysical Research*, 115, E00E16. <https://doi.org/10.1029/2009JE003413>
- Fenton, L. K., & Lorenz, R. (2015). Dust devil height and spacing with relation to the Martian planetary boundary layer thickness. *Icarus*, 260, 246–262. <https://doi.org/10.1016/j.icarus.2015.07.028>
- Fenton, L., Reiss, D., Lemmon, M., Marticorena, B., Lewis, S., & Cantor, B. (2016). Orbital observations of dust lofted by daytime convective turbulence. *Space Science Reviews*, 203(1), 89–142. <https://doi.org/10.1007/s11214-016-0243-6>
- Forget, F., Hourdin, F., Fournier, R., Hourdin, C., Talagrand, O., Collins, M., et al. (1999). Improved general circulation models of the Martian atmosphere from the surface to above 80 km. *Journal of Geophysical Research*, 104, 24155–24175.
- García, R. F., Kenda, B., Kawamura, T., Spiga, A., Murdoch, N., Lognonne, P. H., et al. (2020). Pressure effects on the SEIS-InSight instrument, improvement of seismic records, and characterization of long period atmospheric waves from ground displacements. *Journal of Geophysical Research: Planets*, 125, e06278. <https://doi.org/10.1029/2019JE006278>

Acknowledgments

All co-authors acknowledge NASA, Center National d'Études Spatiales (CNES) and its partner agencies and institutions (UKSA, SSO, DLR, JPL, IPGP-CNRS, ETHZ, IC, and MPS-MPG), and the flight operations team at JPL, CAB, SISMOC, MSDS, IRIS-DMC, and PDS for providing InSight data. The members of the InSight engineering and operations teams are warmly acknowledged for their dedication and hard work in allowing InSight to perform the numerous measurements used in this study. The first author and all French co-authors acknowledge support from the CNES. Additional funding support was provided by Agence Nationale de la Recherche (ANR-19-CE31-0008-08 MAGIS). The modeling part of this work was granted access to the High-Performance Computing (HPC) resources of Center Informatique National de l'Enseignement Supérieur (CINES) under the allocation A006-0110391 made by Grand Equipement National de Calcul Intensif (GENCI). A portion of this research was carried out at the Jet Propulsion Laboratory, California Institute of Technology, under a contract with the National Aeronautics and Space Administration. Additional work was supported by NASA's InSight Participating Scientist Program. Spanish co-authors acknowledge funding by the Centro de Desarrollo Tecnológico e Industrial (CDTI), Ministerio de Economía y Competitividad, and the Instituto Nacional de Técnica Aeroespacial (INTA). The authors thank John Clinton and the Mars Quake Service for monitoring of the atmospheric events in addition to the seismic events.

- Giersch, S., Brast, M., Hoffmann, F., & Raasch, S. (2019). Toward large-eddy simulations of dust devils of observed intensity: Effects of grid spacing, background wind, and surface heterogeneities. *Journal of Geophysical Research: Atmospheres*, *124*, 7697–7718. <https://doi.org/10.1029/2019JD030513>. Retrieved from <https://agupubs.onlinelibrary.wiley.com/doi/abs/10.1029/2019JD030513>
- Golombek, M., Warner, N. H., Grant, J. A., Hauber, E., Ansan, V., Weitz, C. M., et al. (2020). Geology of the InSight landing site, Mars. *Nature Communications*, *11*(1), 1014. <https://doi.org/10.1038/s41467-020-14679-1>
- Gómez-Elvira, J., Armiens, C., Castañer, L., Domínguez, M., Genzer, M., Gómez, F., et al. (2012). REMS: The environmental sensor suite for the Mars Science Laboratory rover. *Space Science Reviews*, *170*, 583–640. <https://doi.org/10.1007/s11214-012-9921-1>
- Haberle, R., Houben, H. C., Hertenstein, R., & Herdtle, T. (1993). A boundary layer model for Mars: Comparison with Viking Lander and entry data. *Journal of the Atmospheric Sciences*, *50*, 1544–1559.
- Hess, S. L., Henry, R. M., Leovy, C. B., Ryan, J. A., & Tillman, J. E. (1977). Meteorological results from the surface of Mars: Viking 1 and 2. *Journal of Geophysical Research*, *82*, 4559–4574.
- Hinson, D. P., Pätzold, M., Tellmann, S., Hausler, B., & Tyler, G. L. (2008). The depth of the convective boundary layer on Mars. *Icarus*, *198*, 57–66. <https://doi.org/10.1016/j.icarus.2008.07.003>
- Hinson, D. P., Tyler, D., Lewis, S. R., Patzold, M., Tellmann, S., Hausler, B., & Tyler, G. L. (2019). The Martian daytime convective boundary layer: Results from radio occultation measurements and a mesoscale model. *Icarus*, *326*, 105–122. <https://doi.org/10.1016/j.icarus.2019.02.028>
- Holstein-Rathlou, C., Gunnlaugsson, H. P., Merrison, J. P., Bean, K. M., Cantor, B. A., Davis, J. A., et al. (2010). Winds at the Phoenix landing site. *Journal of Geophysical Research*, *115*, E00E18. <https://doi.org/10.1029/2009JE003411>
- Jackson, B., & Lorenz, R. (2015). A multiyear dust devil vortex survey using an automated search of pressure time series. *Journal of Geophysical Research: Planets*, *120*, 401–412. <https://doi.org/10.1002/2014JE004712>
- Jackson, B., Lorenz, R., & Davis, K. (2018). A framework for relating the structures and recovery statistics in pressure time-series surveys for dust devils. *Icarus*, *299*, 166–174. <https://doi.org/10.1016/j.icarus.2017.07.027>
- Kahanpää, H., Newman, C., Moores, J., Zorzano, M.-P., Martín-Torres, J., Navarro, S., et al. (2016). Convective vortices and dust devils at the MSL landing site: Annual variability. *Journal of Geophysical Research: Planets*, *121*, 1514–1549. <https://doi.org/10.1002/2016JE005027>
- Kanak, K. M. (2006). On the numerical simulation of dust devil-like vortices in terrestrial and Martian convective boundary layers. *Geophysical Research Letters*, *33*(19). <https://doi.org/10.1029/2006GL026207>
- Kenda, B., Drilleau, M., Garcia, R. F., Kawamura, T., Murdoch, N., & Compaire, N. (2020). Subsurface structure at the InSight landing site from compliance measurements by seismic and meteorological experiments. *Journal of Geophysical Research: Planets*, *125*, e06387. <https://doi.org/10.1029/2020JE006387>
- Kenda, B., Lognonné, P., Spiga, A., Kawamura, T., Kedar, S., Banerdt, W. B., et al. (2017). Modeling of ground deformation and shallow surface waves generated by Martian dust devils and perspectives for near-surface structure inversion. *Space Science Reviews*, *211*, 501–524. <https://doi.org/10.1007/s11214-017-0378-0>
- Kurgansky, M. V. (2019). On the statistical distribution of pressure drops in convective vortices: Applications to Martian dust devils. *Icarus*, *317*, 209–214. <https://doi.org/10.1016/j.icarus.2018.08.004>
- Kurgansky, M. V., Montecinos, A., Villagran, V., & Metzger, S. M. (2011). Micrometeorological conditions for dust-devil occurrence in the Atacama Desert. *Boundary-Layer Meteorology*, *138*(2), 285–298. <https://doi.org/10.1007/s10546-010-9549-1>
- Larsen, S. E., JØrgensen, H. E., Landberg, L., & Tillman, J. E. (2002). Aspects of the atmospheric surface layers on Mars and Earth. *Boundary-Layer Meteorology*, *105*, 451–470. <https://doi.org/10.1023/A:1020338016753>
- Lognonné, P., Banerdt, W. B., Pike, W. T., Giardini, D., Christensen, U., & Garcia, R. F., et al. (2020). Constraints on the shallow elastic and anelastic structure of Mars from InSight seismic data. *Nature Geoscience*, *13*(3), 213–220. <https://doi.org/10.1038/s41561-020-0536-y>
- Lorenz, R. (2011). On the statistical distribution of dust devil diameters. *Icarus*, *215*, 381–390. <https://doi.org/10.1016/j.icarus.2011.06.005>
- Lorenz, R. D. (2012). Observing desert dust devils with a pressure logger. *Geoscientific Instrumentation, Methods and Data Systems*, *1*(2), 209–220. <https://doi.org/10.5194/gi-1-209-2012>
- Lorenz, R. D., Balme, M. R., Gu, Z., Kahanpää, H., Klose, M., Kurgansky, M. V., et al. (2016). History and applications of dust devil studies. *Space Science Reviews*, *203*, 5–37. <https://doi.org/10.1007/s11214-016-0239-2>
- Lorenz, R. D., Lemmon, M., Maki, J., Banfield, D., Spiga, A., Charalambous, C., et al. (2020a). Scientific observations with the insight solar arrays: Dust, clouds and eclipses on Mars. *Earth and Space Science*, *7*(5), e2019EA000992. <https://doi.org/10.1029/2019EA000992>
- Lorenz, R. D., Spiga, A., Lognonne, P., Plasman, M., Newman, C. E., & Charalambous, C. (2020b). The whirlwinds of Elysium: A catalog and meteorological characteristics of “dust devil” vortices observed by Insight on Mars. *Icarus*, *355*. <https://doi.org/10.1016/j.icarus.2020.114119>. Retrieved from <https://www.sciencedirect.com/science/article/pii/S0019103520304632>
- Madeleine, J.-B., Forget, F., Millour, E., Montabone, L., & Wolff, M. J. (2011). Revisiting the radiative impact of dust on Mars using the LMD Global Climate Model. *Journal of Geophysical Research*, *116*, 11010. <https://doi.org/10.1029/2011JE003855>
- Maki, J. N., Golombek, M., Deen, R., Abarca, H., Sorce, C., Goodsall, T., et al. (2018). The color cameras on the InSight lander. *Space Science Reviews*, *214*(6), 105. <https://doi.org/10.1007/s11214-018-0536-z>
- Martinez, G. M., Newman, C. N., De Vicente-Retortillo, A., Fischer, E., Renno, N. O., Richardson, M. I., et al. (2017). The modern near-surface Martian climate: A review of in-situ meteorological data from Viking to curiosity. *Space Science Reviews*, *212*(1), 295–338. <https://doi.org/10.1007/s11214-017-0360-x>
- Mason, P. (1989). Large-eddy simulation of the convective atmospheric boundary layer. *Journal of the Atmospheric Sciences*, *46*(11), 1492–1516.
- Michaels, T. I. (2006). Numerical modeling of Mars dust devils: Albedo track generation. *Geophysical Research Letters*, *33*(19). <https://doi.org/10.1029/2006GL026268>
- Michaels, T. I., & Raffkin, S. C. R. (2004). Large eddy simulation of atmospheric convection on Mars. *Quarterly Journal of the Royal Meteorological Society*, *130*, 1251–1274. <https://doi.org/10.1256/qj.02.169>
- Millour, E., Forget, F., Spiga, A., Navarro, T., Madeleine, J.-B., Montabone, L., et al. (2015). The Mars Climate Database (MCD version 5.2). *European Planetary Science Congress*, *10*, EPSC2015-438.
- Moeng, C., Dudhia, J., Klemp, J., & Sullivan, P. (2007). Examining two-way grid nesting for large eddy simulation of the PBL using the WRF Model. *Monthly Weather Review*, *135*(6), 2295–2311.
- Mueller, N., Knollenberg, J., Grott, M., Kopp, E., Walter, I., Krause, C., et al. (2020). Calibration of the HP³ radiometer on insight. *Earth and Space Science*, *7*(5), e2020EA001086. <https://doi.org/10.1029/2020EA001086>
- Murdoch, N., Kenda, B., Kawamura, T., Spiga, A., Lognonne, P., Mimoun, D., & Banerdt, W. B. (2017). Estimations of the seismic pressure noise on mars determined from large eddy simulations and demonstration of pressure decorrelation techniques for the insight mission. *Space Science Reviews*, *211*, 457–483. <https://doi.org/10.1007/s11214-017-0343-y>

- Murphy, J. R., & Nelli, S. (2002). Mars Pathfinder convective vortices: Frequency of occurrence. *Geophysical Research Letters*, *29*(23), 230000-1.
- Murphy, J., Steakley, K., Balme, M., Deprez, G., Esposito, F., Kahanpaa, H., et al. (2016). Field measurements of terrestrial and Martian dust devils. *Space Science Reviews*, *203*(1), 39–87. <https://doi.org/10.1007/s11214-016-0283-y>
- Newman, C. E., Gomez-Elvira, J., Marin, M., Navarro, S., Torres, J., Richardson, M. I., et al. (2017). Winds measured by the Rover Environmental Monitoring Station (REMS) during the Mars Science Laboratory (MSL) rover's Bagnold Dunes Campaign and comparison with numerical modeling using MarsWRF. *Icarus*, *291*(Suppl C), 203–231. <https://doi.org/10.1016/j.icarus.2016.12.016>. Retrieved from <http://www.sciencedirect.com/science/article/pii/S0019103516304699>
- Newman, C. E., Kahanpaa, H., Richardson, M. I., Martinez, G. M., Vicente-Retortillo, A., & Lemmon, M. T. (2019). MarsWRF convective vortex and dust devil predictions for Gale crater over 3 Mars years and comparison with MSL-REMS observations. *Journal of Geophysical Research: Planets*, *124*, 3442–3468. <https://doi.org/10.1029/2019JE006082>
- Nishizawa, S., Odaka, M., Takahashi, Y. O., Sugiyama, K.-I., Nakajima, K., Ishi-Watari, M., et al. (2016). Martian dust devil statistics from high-resolution large-eddy simulations. *Geophysical Research Letters*, *43*(9), 4180–4188. <https://doi.org/10.1002/2016GL068896>
- Ordóñez-Etxebarria, I., Hueso, R., & Sanchez-Lavega, A. (2018). A systematic search of sudden pressure drops on Gale crater during two Martian years derived from MSL/REMS data. *Icarus*, *299*, 308–330. <https://doi.org/10.1016/j.icarus.2017.07.032>
- Perrin, C., Rodriguez, S., Jacob, A., Lucas, A., Spiga, A., Murdoch, R., et al. (2020). Monitoring of dust-devil tracks around the insight landing site, mars, and comparison with in-situ atmospheric data. *Geophysical Research Letters*, *47*(10), e2020GL087234. <https://doi.org/10.1029/2020GL087234>
- Petrosyan, A., Galperin, B., Larsen, S. E., Lewis, S. R., Maattanen, A., Read, P. L., et al. (2011). The Martian atmospheric boundary layer. *Reviews of Geophysics*, *49*, 3005. <https://doi.org/10.1029/2010RG000351>
- Rafkin, S. C. R., Pla-Garcia, J., Kahre, M., Gomez-Elvira, J., Hamilton, V. E., Marin, M., et al. (2016). The meteorology of Gale Crater as determined from Rover Environmental Monitoring Station observations and numerical modeling. Part II: Interpretation. *Icarus*, *280*, 114–138. <https://doi.org/10.1016/j.icarus.2016.01.031>
- Reiss, D., & Lorenz, R. D. (2016). Dust devil track survey at Elysium Planitia, Mars: Implications for the InSight landing sites. *Icarus*, *266*, 315–330. <https://doi.org/10.1016/j.icarus.2015.11.012>
- Reiss, D., Spiga, A., & Erkeling, G. (2014). The horizontal motion of dust devils on Mars derived from CRISM and CTX/HIRISE observations. *Icarus*, *227*, 8–20. <https://doi.org/10.1016/j.icarus.2013.08.028>
- Renno, N. O., Burkett, M. L., & Larkin, M. P. (1998). A simple thermodynamical theory for dust devils. *Journal of the Atmospheric Sciences*, *55*, 3244–3252.
- Savijarvi, H. (1999). A model study of the atmospheric boundary layer in the Mars Pathfinder lander conditions. *Quarterly Journal of the Royal Meteorological Society*, *125*(554), 483–493.
- Schofield, J. T., Crisp, D., Barnes, J. R., Haberle, R. M., Magalhaes, J. A., Murphy, J. R., et al. (1997). The Mars Pathfinder atmospheric structure investigation/meteorology (ASI/MET) experiment. *Science*, *278*, 1752–1757.
- Skamarock, W. C., & Klemp, J. B. (2008). A time-split nonhydrostatic atmospheric model for weather research and forecasting applications. *Journal of Computational Physics*, *227*, 3465–3485. <https://doi.org/10.1016/j.jcp.2007.01.037>
- Smith, M. D., Wolff, M. J., Spanovich, N., Ghosh, A., Banfield, D., Christensen, P. R., et al. (2006). One Martian year of atmospheric observations using MER Mini-TES. *Journal of Geophysical Research*, *111*(E12). <https://doi.org/10.1029/2006JE002770>
- Spiga, A. (2020). A study of daytime convective vortices and turbulence in the Martian planetary boundary layer based on half-a-year of insight atmospheric measurements and large-eddy simulations [data set]. *ESPRI/IPSL*. <https://doi.org/10.14768/2DDABA56-CF61-4D5B-83B7-E4A079ED836B>
- Spiga, A. (2012). Comment on “observing desert dust devils with a pressure logger” by Lorenz (2012) – Insights on measured pressure fluctuations from large-eddy simulations. *Geoscientific Instrumentation, Methods and Data Systems*, *1*(2), 151–154. <https://doi.org/10.5194/gi-1-151-2012>. Retrieved from <https://www.geosci-instrum-method-data-syst.net/1/151/2012/>
- Spiga, A., Banfield, D., Teanby, N. A., Forget, F., Lucas, A., Kenda, B., et al. (2018). Atmospheric science with InSight. *Space Science Reviews*, *214*, 109. <https://doi.org/10.1007/s11214-018-0543-0>
- Spiga, A., Barth, E., Gu, Z., Hoffmann, F., Ito, J., Jemmett-Smith, B., et al. (2016). Large-eddy simulations of dust devils and convective vortices. *Space Science Reviews*, *203*, 245–275. <https://doi.org/10.1007/s11214-016-0284-x>
- Spiga, A., & Forget, F. (2009). A new model to simulate the Martian mesoscale and microscale atmospheric circulation: Validation and first results. *Journal of Geophysical Research*, *114*, E02009. <https://doi.org/10.1029/2008JE003242>
- Spiga, A., Forget, F., Lewis, S. R., & Hinson, D. P. (2010). Structure and dynamics of the convective boundary layer on Mars as inferred from large-eddy simulations and remote-sensing measurements. *Quarterly Journal of the Royal Meteorological Society*, *136*, 414–428. <https://doi.org/10.1002/qj.563>
- Spiga, A., Forget, F., Madeleine, J., Montabone, L., Lewis, S. R., & Millour, E. (2011). The impact of Martian mesoscale winds on surface temperature and on the determination of thermal inertia. *Icarus*, *212*, 504–519.
- Spohn, T., Grott, M., Smrekar, S. E., Knollenberg, J., Hudson, T. L., Krause, C., et al. (2018). The heat flow and physical properties pack-age (HP³) for the InSight mission. *Space Science Reviews*, *214* (5), 96. <https://doi.org/10.1007/s11214-018-0531-4>
- Steakley, K., & Murphy, J. (2016). A year of convective vortex activity at Gale Crater. *Icarus*, *278*, 180–193. <https://doi.org/10.1016/j.icarus.2016.06.010>
- Tillman, J. E., Landberg, L., & Larsen, S. E. (1994). The boundary layer of Mars: Fluxes stability, turbulent spectra and growth of the mixed layer. *Journal of the Atmospheric Sciences*, *51* (12), 1709–1727.
- Toigo, A. D., & Richardson, M. I. (2003). Meteorology of proposed Mars exploration rover landing sites. *Journal of Geophysical Research*, *108*(E12), 8092. <https://doi.org/10.1029/2003JE002064>
- Torrence, C., & Compo, G. P. (1998). A practical guide to wavelet analysis. *Bulletin of the American Meteorological Society*, *79*(1), 61–78.
- Víudez-Moreiras D., Newman C. E., Forget F., Lemmon M., Banfield D., Spiga A., Lepinette J. A., et al. (2020). Effects of a large dust storm in the near-surface atmosphere as measured by InSight in Elysium Planitia, Mars. Comparison with contemporaneous measurements by Mars Science Laboratory. *Journal of Geophysical Research: Planets*, *125*, e2020JE006493. <https://doi.org/10.1029/2020JE006493>. Retrieved from <https://agupubs.onlinelibrary.wiley.com/doi/abs/10.1029/2020JE006493> (e2020JE0064932020JE006493)
- Víudez-Moreiras, D., Gomez-Elvira, J., Newman, C. E., Navarro, S., Marin, M., Torres, J., et al. (2019). Gale surface wind characterization based on the Mars Science Laboratory REMS dataset. Part I: Wind retrieval and Gale's wind speeds and directions. *Icarus*, *319*, 909–925. <https://doi.org/10.1016/j.icarus.2018.10.011>
- Willis, G., & Deardorff, J. (1979). Laboratory observations of turbulent penetrative-convection planforms. *Journal of Geophysical Research*, *84*, 295–302.